

IDEA League

MASTER OF SCIENCE IN APPLIED GEOPHYSICS
RESEARCH THESIS

A wave-equation based AVO inversion of VSP and surface seismic data

Veerle Steenhuisen

August 19, 2016

A wave-equation based AVO inversion of VSP and surface seismic data

MASTER OF SCIENCE THESIS

for the degree of Master of Science in Applied Geophysics at

Delft University of Technology

ETH Zürich

RWTH Aachen University

by

Veerle Steenhuisen

August 19, 2016

Department of Geoscience & Engineering	·	Delft University of Technology
Department of Earth Sciences	·	ETH Zürich
Faculty of Georesources and Material Engineering	·	RWTH Aachen University



Delft University of Technology

Copyright © 2016 by IDEA League Joint Master's in Applied Geophysics:

Delft University of Technology

All rights reserved.

No part of the material protected by this copyright notice may be reproduced or utilized in any form or by any means, electronic or mechanical, including photocopying or by any information storage and retrieval system, without permission from this publisher.

Printed in The Netherlands

IDEA LEAGUE
JOINT MASTER'S IN APPLIED GEOPHYSICS

Delft University of Technology, The Netherlands
ETH Zürich, Switzerland
RWTH Aachen, Germany

Dated: *August 19, 2016*

Supervisors:

dr.ir. P. Haffinger

ir. A.K.T. Wever

prof.dr.ir. C.P.A. Wapenaar

Committee Members:

ir. A.K.T. Wever

prof.dr.ir. C.P.A. Wapenaar

prof.dr.ir. J.F. Wellmann

Abstract

Seismic data are acquired by sending band-limited sound waves into the earth, where they are reflected at boundaries of geological layers and by measuring these reflections at the earth's surface. Geophysical processing of seismic data results in a structural image of the subsurface. At present, apart from structural information, knowledge of the material properties of the subsurface is required to predict the risk of a target to be commercially attractive or not. Through inversion techniques these material properties can be obtained.

An inversion algorithm developed by Delft Inversion is applied to synthetic, VSP and surface seismic data provided by Wintershall Noordzee, in order to obtain the bulk and shear moduli distributions within the area of investigation, which is situated in the Anglo-Dutch Basin. This inversion algorithm takes the non-linear relationship between seismic data and reservoir properties into account, involving multiple scattering, mode conversions and exact travel-times.

As outcome, the inversion of synthetic data computed from real well logs resulted in an excellent match of the inversion results with the modelled data, provided that the synthetic data were modelled in the pre-stack domain and with a broadband wavelet. Furthermore, the surface seismic data quality was found to be of a too low quality to provide high-resolution reservoir characterisation. Nevertheless, high-compressibility features present in the seismic inversion results, could be interpreted as sandstone layers.

Acknowledgements

First of all, I want to thank all the people who were directly and indirectly involved in this project.

Dear Peter, Andries and Kees, thank you for your support, sincere interest and for making me feel comfortable and welcome to ask you for advice; I greatly appreciate having you as supervisors.

Panos, thank you for your patience in helping me out with the software and making me feel at home in the Delft Inversion office.

Dries, thank you for all the interesting (scientific) discussions and your eagerness to explain any theoretical background.

Marc, thank you for your thorough explanations and quick responses regarding the data obtained from Wintershall.

Many thanks to Wintershall Noordzee B.V. for providing me with real data to investigate this topic.

All Applied Geophysics employees and scientific staff, thank you for setting up, maintaining and improving this programme. The past two years have been a great experience.

And finally, but most importantly, my family and friends; thank you for your listening ear, your endless support and love. You make my life extraordinary.

Delft University of Technology
August 19, 2016

Veerle Steenhuisen

Table of Contents

Abstract	v
Acknowledgements	vii
Nomenclature	xix
Acronyms	xxi
1 Introduction	1
I Rock Physics Analysis	3
2 Well data	5
2-1 Geological overview	5
2-2 Well logs	6
2-3 Lithological description	7
2-4 Crossplots	7
3 Gassmann fluid substitution	11
3-1 Gassmann's equations	11
3-2 Results	12
4 Compressibility sensitivity analysis	15
4-1 Critical concentration model	15
4-2 Results	15

II	Synthetics and Multiple Prediction	17
5	Synthetic gathers	19
5-1	Kennett invariant embedding method	19
5-2	Results	20
6	Multiple prediction	25
6-1	Multiple theory	25
6-2	Data preparation and approach	25
6-3	Results	26
III	Seismic data and seismic-to-well tie	29
7	VSP data	31
7-1	VSP technique	31
7-2	VSP data	31
8	Surface seismic data	33
8-1	Post-stack time-migrated seismic data	33
8-2	Pre-stack depth-migrated seismic data	33
9	VSP-to-well tie	35
9-1	Seismic-to-well tie technique	35
9-2	Results	36
10	Seismic-to-well tie	39
10-1	Results	39
IV	Wave-equation based AVO inversion	45
11	The inversion algorithm	47
11-1	Inverse theory	47
11-2	The wave-equation based AVO inversion	48
12	Synthetic inversion	49
12-1	Results	49
13	VSP inversion	53
13-1	Data preparation and approach	53
13-2	Results	53
14	Surface seismic inversion	57
14-1	Data preparation and approach	57
14-2	Results	58

Table of Contents xi

15 Conclusions	67
Bibliography	69
A Critical concentration model	71
B Linear regression model	73

List of Figures

2-1	Crossplots over the interval 3648 - 3839m MD.	8
2-2	Crossplot of compressibility versus shear compliance, coloured by reservoir type.	9
3-1	Crossplots of compressibility versus shear compliance, coloured by target gas saturation, for all fluid substituted depth samples in reservoir <i>LWC1</i> and reservoir <i>LWC5</i>	12
3-2	Average compressibility of all depth samples within reservoir <i>LWC1</i> and reservoir <i>LWC5</i> as a function of the target gas saturation after Gassmann fluid substitution has been applied to those samples.	13
4-1	Compressibility as a function of the endmember sand porosity and gas saturation, modelled for reservoir <i>LWC1</i> , which is calculated to have an average critical porosity of 30%.	16
5-1	Four incident P- and S- waves illuminating a horizontally layered medium from above and below and the four resulting P- and S-waves after reflection, transmission and/or conversion of the incident waves.	20
5-2	Synthetic PP gathers in migrated time over the interval 3510 - 3840m MD, modelled with a 7-12-40-50Hz bandpass filtered wavelet. The left gather is modelled for the fluid substituted log data with a target gas saturation of 80% in reservoir <i>LWC5</i> (effective porosity of 16%), the middle gather is modelled for the original log data, where the gas saturation in reservoir <i>LWC5</i> is 12%, and the right gather shows the difference between the previous two gathers. The pink arrow indicates the approximate location of reservoir <i>LWC1</i> and the orange arrow that of reservoir <i>LWC5</i>	21
5-3	Synthetic PP gathers in migrated time over the interval 3510 - 3840m MD, modelled with a 7-12-40-50Hz bandpass filtered wavelet. The left gather is modelled for the fluid substituted log data with a target gas saturation of 80% in reservoir <i>LWC1</i> (effective porosity of 9.9%), the middle gather is modelled for the fluid substituted log data with a target gas saturation of 10% in reservoir <i>LWC1</i> and the right gather shows the difference between the previous two gathers.	22

5-4	Synthetic PP gathers in migrated time over the interval 3510 - 3840m MD, modelled with a 7-12-40-50Hz bandpass filtered wavelet. On the left is the synthetic gather modelled for a 30% increased target bulk porosity (compared to the original bulk porosity) in reservoir <i>LWC5</i> , the middle gather is modelled for the original log data and the right gather shows the difference between the previous two gathers.	23
6-1	The final 250ms of the synthetic PP gathers in migrated time over the interval 2100 - 3840m MD, that were modelled with a 7-12-40-50Hz bandpass filtered wavelet. On the left is the synthetic gather modelled for the original log data and on the right the synthetic gather modelled for the 'extended overburden' log data.	27
6-2	The total wavefield for the 'extended overburden' and original log data in virtual VSP display.	28
7-1	A typical onshore VSP survey with the source on the surface and the receivers inside the borehole [Blackburn et al., 2007].	32
7-2	VSP corridor stack, limited to a time window of 1700 - 2500 ms.	32
9-1	Results for the most optimal seismic-to-well tie of the VSP data with the synthetic data over the interval 2100 - 3840m MD.	37
9-2	Results for the most optimal seismic-to-well tie of the VSP data with the synthetic data over the interval 3300 - 3840m MD.	38
10-1	Results for the most optimal seismic-to-well tie of the seismic post-stack data with the synthetic data over the interval 2100 - 3840m MD.	40
10-2	Results for the most optimal seismic-to-well tie of the seismic post-stack data with the synthetic data over the interval 3300 - 3840m MD.	41
10-3	Results for the most optimal seismic-to-well tie of the seismic pre-stack data with the synthetic data over the interval 2100 - 3840m MD.	42
10-4	Results for the most optimal seismic-to-well tie of the seismic pre-stack data with the synthetic data over the interval 3300 - 3840m MD.	43
11-1	A flow diagram describing the non-linear inversion algorithm developed by Delft Inversion [Haffinger et al., 2015].	48
12-1	Inversion results (in blue) of compressibility with depth for the synthetic gathers that were modelled for a zero-offset slowness range, but each with a different wavelet, over the interval 3300 - 3840m MD. In black are the original compressibility log curves, which have been anti-alias filtered for 8m sampling.	50
12-2	Inversion results (in blue) of compressibility and shear compliance with depth, for the synthetic gathers that were modelled for a pre-stack slowness range, but each with a different wavelet, over the interval 3300 - 3840m MD. In black are the original compressibility and shear compliance log curves, which have been anti-alias filtered for 8m sampling.	51
12-3	Inversion result (in blue) of compressibility with depth for the synthetic gather that was modelled over the interval 2100 - 3840m MD, for the original log data. In black is the original compressibility log curve, which has been anti-alias filtered for 8m sampling.	52
13-1	Inversion result (in blue) of compressibility with depth for the VSP corridor stack. The blue curve is the inversion result itself, the black curves is the smooth log and the red curve is the background log. The black arrows indicate the approximate locations of three Carboniferous reservoirs.	54

13-2	The VSP corridor stack (left), the synthetic gather that is the result of convolution of the inversion results with the extracted wavelet (centre) and the residual gather (right) which is magnified by a factor 2.	55
14-1	Inversion result (in blue) of compressibility with depth for the post-stack seismic data. The blue curve is the inversion result itself, the black curve is the smooth log and the red curve is the background log. The black arrows indicate the approximate locations of three Carboniferous reservoirs.	59
14-2	The post-stack seismic gather, the synthetic gather that is the result of convolution of the inversion results with the extracted wavelet (centre) and the residual gather (right) which is magnified by a factor 2.	59
14-3	3D plot of the compressibility distribution as a result of the post-stack seismic data inversion over the interval 3300 - 3900m MD. Displayed are the inline and crossline that run through the well location. The reservoirs <i>LWC5</i> and <i>EWC8</i> are indicated by arrows.	60
14-4	Depth slices showing the compressibility distribution as a result of the post-stack seismic data inversion over the interval 3300 - 3900m MD.	61
14-5	Inversion results (in blue) of compressibility and shear compliance with depth for the pre-stack seismic data. The blue curves are the inversion result itself, the black curves are the smooth logs and the red curves are the background logs. The black arrows indicate the approximate locations of three Carboniferous reservoirs.	62
14-6	The pre-stack seismic gather, the synthetic gather that is the result of convolution of the inversion results with the extracted wavelet (centre) and the residual gather (right) which is magnified by a factor 2.	63
14-7	3D plot of the compressibility distribution as a result of the pre-stack seismic data inversion over the interval 3320 - 3850m MD. Displayed are the inline and crossline that run through the well location. Reservoirs <i>LWC5</i> and <i>EWC8</i> are indicated by arrows.	64
14-8	Depth slices showing the compressibility distribution as a result of the pre-stack seismic data inversion over the interval 3320 - 3850m MD.	65

List of Tables

5-1	Goodness-of-fit for each crossplot per reservoir.	23
-----	---	----

Nomenclature

Abbreviations

Ma Megaannus

Greek Symbols

ϕ porosity [-]

ρ density [g/cm^3]

μ shear modulus [N/m^2]

κ compressibility [m^2/N]

Latin Symbols

K bulk modulus [N/m^2]

M shear compliance [m^2/N]

V_p compressional velocity [m/s]

V_s shear velocity [m/s]

Subscripts

min minimum

max maximum

s solid

b bulk

sh shale

fl fluid

sst sandstone

c critical

ctl control

w water

HC hydrocarbon

Acronyms

AVA amplitude versus angle

AVO amplitude versus offset

DSL Digital Spectralog

GR Gamma Ray [API]

HDIL High-Definition Induction Log [Ω]

MD Measured Depth [m]

XMAC Cross Multipole Array Acoustilog

VSP Vertical Seismic Profile

ZDL Z-Densilog

Chapter 1

Introduction

In 1936, the first oilfield discovery was made using seismic exploration [Waterman, 1947]. Seismic exploration is based on the principle of sending band-limited sound waves into the earth, where they are reflected at boundaries of geological layers and measuring these reflected waves at the earth's surface. The acquired seismic data have been used ever since to obtain structural information of the subsurface and therefore determine the location and size of possible oil and gas reservoirs. However, in recent years, structural information alone has become insufficient to detect oil and gas reservoirs. This is due to the fact that most geologically prominent reservoirs have been detected and produced already, leaving the less-obvious and harder-to-detect reservoirs, such as pinch-out or fault-bounded reservoirs, and stratigraphic traps. Consequently, a lot of effort has been put into obtaining material properties of the subsurface from seismic data over the past years. This can be done with a method known as inversion.

Seismic inversion still comes with a lot of challenges however. One of the major issues within the oil and gas industry is to distinguish reservoirs containing residual gas from commercially attractive reservoirs on acoustic impedance data derived from seismic. This is due to the fact that many effects influence acoustic impedance, such as lithology, fluid saturation and porosity. Another reason is the sensitivity of compressional velocity to gas; a small amount of gas already results in a dramatic drop in compressional velocity. Thus, it is generally expected to be impossible to quantify gas saturation on acoustic impedance data only [Russell and Hampson, 2006]. Apart from this, the ambiguous interpretation of acoustic impedance data makes it hard to distinguish tight¹ from non-tight reservoirs.

As a consequence, the idea to invert for a property that is more sensitive to gas saturation and to use additional information in the inversion process was developed, i.e. by Delft Inversion. They developed software, that takes the *non-linear relationship* between seismic data and reservoir properties into account, involving multiple scattering, mode conversions and exact travel-times. Apart from this, the software also solves directly for the bulk and shear moduli

¹A tight reservoir is defined in this context as a reservoir that cannot be produced with conventional technology, typically because of low porosity and/or permeability.

instead of for acoustic and shear impedances, because these elastic properties are much more sensitive to porosity and hydrocarbon saturation [Gisolf and van den Berg, 2012].

In this project I apply the Delft Inversion technology to synthetic, Vertical Seismic Profile (VSP) and surface seismic data provided by Wintershall Noordzee, in which the dataset is believed to contain i.a. tight reservoir rock and/or low-saturation gas reservoirs. By comparing results obtained from VSP data (which can be processed in such a way that they are multiple free) with those from surface seismic data, I will verify the impact that multiples have on the seismic characterisation of the reservoir. Apart from this I will attempt to clarify whether it is possible to predict the risk of a target to be tight and/or filled with low-saturation gas.

Part I

Rock Physics Analysis

Chapter 2

Well data

Well logs provide an in-situ measurement of elastic rock properties. In this chapter, a Rock Physics Analysis is done to get an idea of how different lithologies and reservoir intervals can be characterised on such well log data. In addition, a geological overview of the area around the well location is given and the well data itself are described.

2-1 Geological overview

The area of investigation is situated in the Anglo-Dutch Basin, in the Southern North Sea, which has developed as a result of a long and complex history of subsidence and uplift. The basin is underlain by a thick basement of Lower Palaeozoic age (590 - 250 Ma ago), that was mildly deformed during the Caledonian Orogeny in Late Silurian to Early Devonian times (420 - 390 Ma ago). After this uplift, most of the basin remained an upland area of net erosion during the Devonian about 410 - 360 million years ago. Early in the Carboniferous, approximately 360 million years ago, crustal extension started, resulting in the deposition of deep-water and deltaic sediments within the grabens.

Then another orogeny occurred between 300 - 290 million years ago, the Variscan Orogeny, during which the Carboniferous rocks were gently folded and faulted. Following this orogeny, the basin began to subside again in the Permian (290 - 250 Ma ago), resulting in the deposition of a thick cyclical evaporite succession, also known as the Zechstein supergroup.

In the Late Triassic (230 - 200 Ma ago), the Variscan basement faults were reactivated, triggering halokinesis of the Permian evaporites. Fully marine conditions were re-established at the end of the Triassic and thick sandstone packages were deposited in the form of alluvial fans. Subsequently, widespread domal uplift in the Jurassic (200 - 150 Ma ago) resulted in an unconformity and the erosion of more than 1000m of Jurassic and Triassic strata. During the Cretaceous about 150 - 65 million years ago, the climate was relatively warm, resulting in the deposition of a thick succession of carbonates. For the rest of the Cenozoic era, mostly subsidence occurred, resulting in the deposition of sequences of deltaic shales and sandstones and the reactivation of basement faults. [Balson et al., 2001]

2-2 Well logs

The near vertical well X was drilled as an exploration well, with the objective of proving gas in Carboniferous fluvial sandstones. It was originally classified as "dry", meaning that the well didn't encounter any (commercial amounts of) gas. However, log characteristics are suspicious and a Free Water Level is suspected to be lower than previously thought.

For the analysis I used the following log curves:

- A Gamma Ray [API] (GR) log curve, that was measured with the GR and Digital Spectralog (DSL) tools [BHc, 2014] over the entire length of the borehole from 68.7m Measured Depth [m] (MD) until 3846m MD. I used the GR log as a lithology indicator and to calculate the shale volume percentage from.
- A resistivity log curve, that was obtained with the High-Definition Induction Log [Ω] (HDIL) tool [BHc, 2014], run over the target interval only, from 3500m MD until 3846.3m MD. The resistivity log was used as a fluid indicator and to determine the water saturation from.
- A compressional sonic log curve, that was measured with the Cross Multipole Array Acoustilog (XMAC) tool [BHc, 2014] over the interval 1000 - 3846.3m MD. I used the sonic log a.o. for the creation of synthetic gathers.
- A shear sonic log curve, that was measured with the XMAC tool [BHc, 2014] over the interval 1000 - 3846.3m MD. I used the shear sonic log a.o. for the creation of synthetic gathers.
- A density log curve, that was measured with the Z-Densilog (ZDL) tool [BHc, 2014] over the target interval only, from 3500m MD until 3846.3m MD. The density was used a.o. for the creation of synthetic gathers and to determine the porosity.

As can be seen from the above, the majority of tools were only run over the target interval. Apart from this, the XMAC tool was run through casing over the interval 2507 - 3519m MD. Logging behind casing comes with a much higher uncertainty than logging in an open hole, as has been done over the target interval. This is due to the fact that a good cement bond is required to provide the necessary acoustic coupling to the formation and to eliminate the casing arrival [Chen and Eriksen, 1991]. Furthermore, the XMAC tool did not record sonic travel-times over a large part within the Zechstein formation, according to the composite log description.

In order to do a thorough multiple prediction later on, compressional, shear sonic and density log curves are needed, both over the reservoir section as well as the overburden containing the multiple generators. To obtain this, a 3-layered neural network was used to predict these log curves over the entire borehole. This neural network prediction was done in PETREL with as input the sonic (through casing) log curves (where available), GR log curve, zone log and all available sonic and density log curves of wells in the surrounding area. The neural network effectively does a shale-compensated calibrated Gardner transformation (when applied to the density log). Finally, the predicted log curves were merged with the original log curves, to fill any gaps in the original log curves.

Nevertheless, extremely high sonic travel-time readings (i.e. low velocity readings) at three distinct intervals within the Zechstein remained present in the log data. I found this suspicious, because the information from the cuttings and the GR log curve show no sign that such low-velocity intervals exist. Apart from this, velocities of less than 3000m/s at a depth of 3000m are hard to explain. A possible explanation for these low-velocity intervals could be that polyhydrate salts occur at these locations. When these salts are in contact with water-based mud, as used in this particular well, severe dissolution occurs, resulting in invalid readings of the tool. Because of this, I decided to clear the three low velocity intervals from the logs and to replace them with constant values for corresponding salt minerals given in the composite log description.

2-3 Lithological description

Well X encountered the following lithostratigraphic units from the top (68.7m MD) to the bottom (3852m MD):

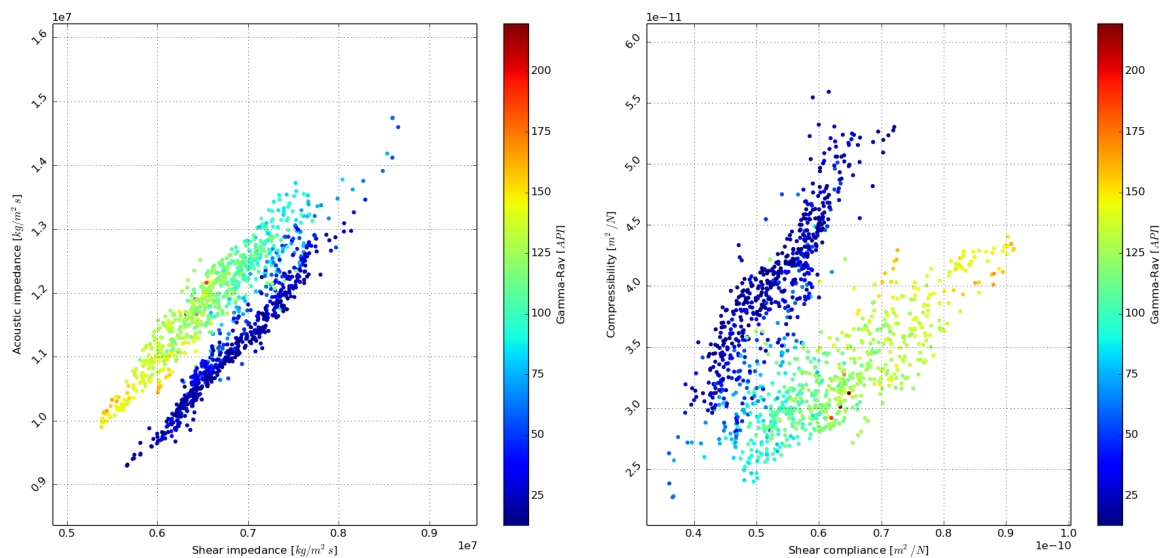
- North Sea Group, which consists largely of interbedded Tertiary claystones and sandstones;
- Chalk Group, a thick package of mostly chalk with occasional chert layers, deposited throughout the Cretaceous;
- Rijnsland Group, consisting of thin layers of Cretaceous marl, limestone and claystone;
- Scruff Group, consisting of a very thin package of the Late Jurassic Kimmeridge claystone;
- Upper Germanic Trias Group, a unit in which alternatingly claystone, dolomite and evaporite layers are present;
- Lower Germanic Trias Group, consisting of a sequence of claystone, evaporite and sandstone layers, followed by a thick package of Bunter sandstone;
- Zechstein Group, a unit of almost 1000m thick, that consists of cyclical evaporite successions, in which a.o. halite, anhydrite and potassium magnesium salt are observed;
- Upper Rotliegend Group, containing mostly Permian claystone with occasional sandstone layers;
- Limburg Group, which consists of the Carboniferous fluvial Westphalian sandstones, the reservoirs of interest for this study.

2-4 Crossplots

First of all, I started crossplotting several properties against each other over an interval containing the reservoirs of interest, 3648 - 3839m MD. In Figure 2-1 two crossplots are shown: a crossplot of acoustic impedance versus shear impedance coloured by GR on the left

(2-1a) and a crossplot of compressibility¹ versus shear compliance² coloured by GR on the right (2-1b). Two distinct groups of data can be identified in both crossplots, each with a very clear and nearly linear trend. Higher acoustic impedance and compressibility result in increasing shear impedance and shear compliance, respectively. Low GR values (blue colours) indicate sands, whereas high GR values (green to red colours) indicate shales. The crossplot of compressibility versus shear compliance allows for a better discrimination between these two lithological classes, because in this crossplot the sand and shale trends are better separated. It should be noted that the relative position of the sand-group differs in the two crossplots.

From the crossplots in Figure 2-1 it can also be seen that two parameters are needed in order to make a proper separation between the lithological groups. Compressibility alone would not be sufficient to obtain information on the lithology type. Based on the above mentioned observations, I selected only compressibility and shear compliance for further crossplots.



(a) Crossplot of acoustic impedance versus shear impedance, coloured by GR. (b) Crossplot of compressibility versus shear compliance, coloured by GR.

Figure 2-1: Crossplots over the interval 3648 - 3839m MD.

As a next step, I defined all the sandstone reservoirs within the Carboniferous section drilled by well X, using a.o. the Geological Well Summary provided and my petrophysical knowledge. Again I made crossplots of compressibility versus shear compliance for several of these reservoirs, in order to see if the reservoirs could be distinguished from each other based on their elastic properties and in order to see what influenced these elastic properties.

In Figure 2-2, compressibility is crossplotted against shear compliance for all depth samples within reservoir *LWC1* and reservoir *LWC5*³. From the crossplot it can be seen that based on these elastic properties, a clear distinction can be made between the two reservoirs. Reservoirs

¹Compressibility is the inverse of the bulk modulus.

²Shear compliance is the inverse of the shear modulus.

³Reservoir LWC1 and LWC5 are two sandstone layers within the Limburg Group. Further on in this report, these two reservoirs will repeatedly be mentioned and compared.

LWC1 and *LWC5* are both sandstone reservoirs, that hardly contain any shale or higher-GR datapoints. Reservoir *LWC1*, which has an average effective porosity of 9.9% and an average gas saturation of 55%, is plotted in green and reservoir *LWC5*, which has an average effective porosity of 16% and an average gas saturation of 12%, is plotted in orange. Furthermore, the crossplot shows that reservoir *LWC1* has an average compressibility and shear compliance that are lower than for reservoir *LWC5*. Because both an increase in porosity as well as an increase in gas saturation result in an increased compressibility, this observation suggests that in this situation porosity has a greater impact on compressibility than gas saturation.

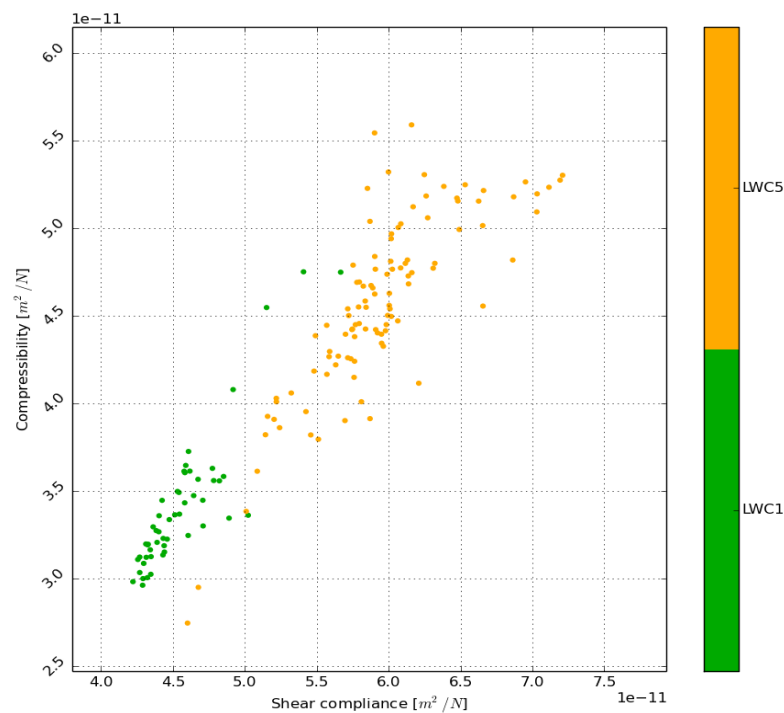


Figure 2-2: Crossplot of compressibility versus shear compliance, coloured by reservoir type.

Gassmann fluid substitution

Because I wanted more confidence that porosity indeed has a greater impact on compressibility compared to gas saturation, I used the Gassmann model for fluid substitution to visualise the effect of increasing gas saturation on the different reservoirs. How this is done will be described in this chapter.

3-1 Gassmann's equations

Gassmann's equations are the most commonly used relations to model the influence of pore fluids on seismic properties. The best indicator of a fluid saturation effect is the bulk modulus (K), which is a function of compressional velocity (V_p), shear velocity (V_s) and bulk density (ρ_b):

$$K = \rho_b(V_p^2 + \frac{4}{3}V_s^2). \quad (3-1)$$

A seismic wave passing through a rock causes an increase in pressure in the fluid filling the pores, which results in a stiffening of the rock and an increase of the bulk modulus. The Gassmann theory predicts the resulting increase in effective bulk modulus of the saturated rock, K_{sat} , through the following equation:

$$\frac{K_{sat}}{K_0 - K_{sat}} = \frac{K_{dry}}{K_0 - K_{dry}} + \frac{K_{fl}}{\phi(K_0 - K_{fl})}, \quad (3-2)$$

with $\mu_{sat} = \mu_{dry}$ and where K_0 is the effective bulk modulus of the mineral material making up the rock, K_{dry} is the effective bulk modulus of the dry rock, K_{fl} is the effective bulk modulus of the rock saturated with pore fluid and ϕ is the porosity. In the Gassmann theory, the shear modulus, μ , is independent of the pore fluid and held constant during the fluid substitutions [Mavko et al., 2009].

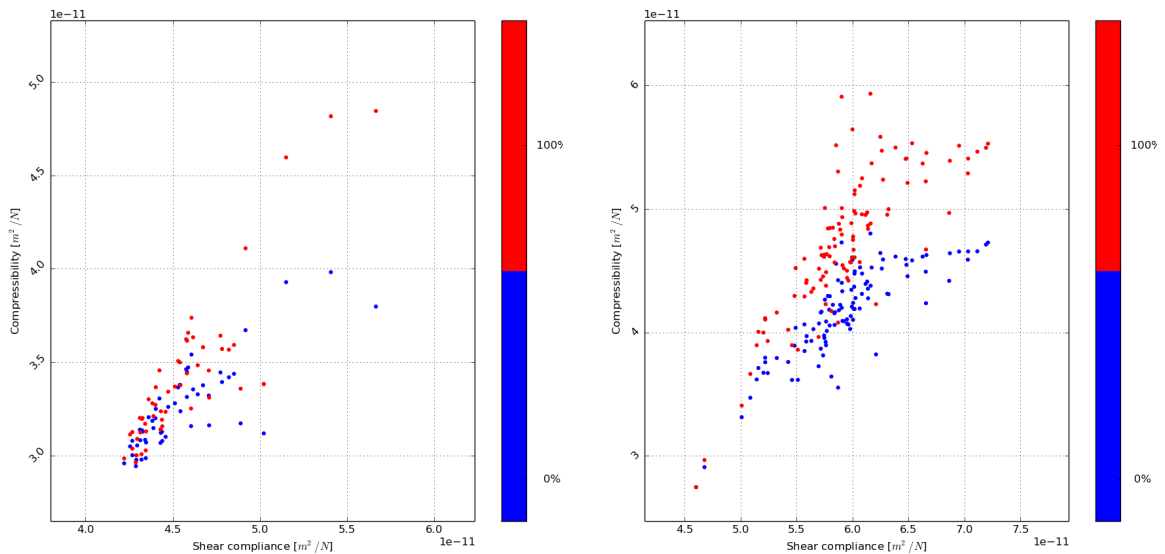
The Gassmann theory involves assumptions, which are:

- The rock is isotropic and homogeneous;
- The pore space is well connected and in pressure equilibrium;
- The porosity of the rock remains constant with different saturating fluids;
- There is no chemical interaction between the fluids and the solids.

To get an idea of the implementation of the Gassmann theory, as used in the Delft Inversion software, please refer to [Kumar, 2006].

3-2 Results

I applied Gassmann's equations (3-2) to reservoir *LWC1*, which has a relatively low effective porosity (9.9%), and to reservoir *LWC5*, which has a relatively high effective porosity (16.0%), thus creating several sets of logs, each with a different target gas saturation in either one of the two reservoirs.



- (a) Data within reservoir *LWC1* (effective porosity of 9.9%) that have been fluid substituted with brine (0% target gas saturation, blue dots) and with gas (100% target gas saturation, red dots). (b) Data within reservoir *LWC5* (effective porosity of 16%) that have been fluid substituted with brine (0% target gas saturation, blue dots) and with gas (100% target gas saturation, red dots).

Figure 3-1: Crossplots of compressibility versus shear compliance, coloured by target gas saturation, for all fluid substituted depth samples in reservoir *LWC1* and reservoir *LWC5*.

Figure 3-1 shows the depth samples within reservoir *LWC1* (Figure 3-1a) and within reservoir *LWC5* (Figure 3-1b), that have been fluid substituted with either brine or gas, crossplotted as a function of compressibility and shear compliance. From these crossplots it can be seen that the elastic properties of the low-porosity sandstone reservoir *LWC1* are less affected by an increasing gas saturation than those of the high-porosity sandstone reservoir *LWC5*.

I verified this by computing the average compressibility over the *LWC1* and *LWC5* intervals, as a function of the target gas saturation after Gassmann fluid substitution has been applied to those intervals (see Figure 3-2). The average compressibility increase between the 0% and 100% gas case is 11.9% for reservoir *LWC5* and 4.7% for reservoir *LWC1*, showing that gas saturation indeed has a larger affect on compressibility for reservoir *LWC5*. In addition, it can also be observed from this figure that for both reservoirs, compressibility increases the most between 0% and 10% gas saturation.

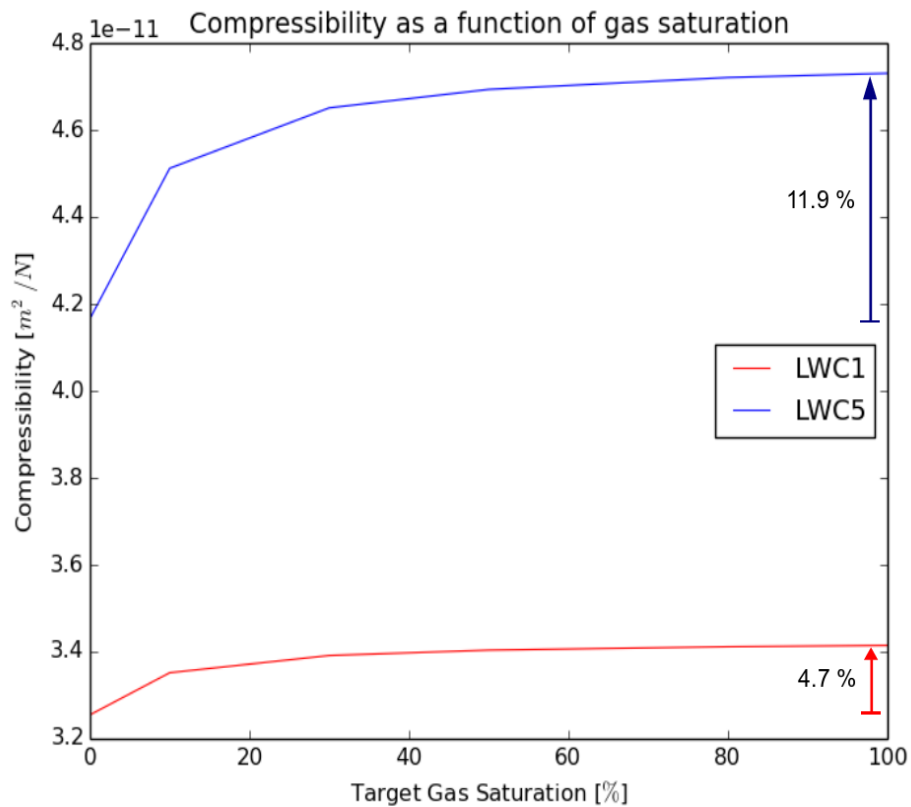


Figure 3-2: Average compressibility of all depth samples within reservoir *LWC1* and reservoir *LWC5* as a function of the target gas saturation after Gassmann fluid substitution has been applied to those samples.

Compressibility sensitivity analysis

In order to see the relative impact of gas saturation and porosity on compressibility, I made 2D plots of compressibility as a function of porosity and gas saturation. Before I could make these plots, I had to find a way to express P- and S-wave velocity as a function of gas saturation and porosity, because compressibility is calculated from the P- and S-wave velocities. This could theoretically be achieved by making use of the critical concentration model, as will be described in this chapter.

4-1 Critical concentration model

With the critical concentration model as described by [Mavko et al., 2009], it is possible to examine the effect that a variable porosity and gas saturation have on the compressibility. This is done with the help of a parameter called the critical porosity, which is the porosity of the sediment at the moment of deposition, so before compaction and diagenesis have taken place.

The critical concentration model is based upon the idea that compressional and shear velocities of rocks should trend between the velocities of the mineral grains in the limit of low porosity and the values for a mineral-pore fluid suspension in the limit of high porosity. Within my adapted version of the model, the assumption is made that the rock consists of shale and sandstone, where only the sandstone can consist of a rock frame and pore network, whereas shale is assumed to have zero effective porosity. For a detailed overview of this model, please refer to Appendix A.

4-2 Results

The compressibility sensitivity plot for reservoir *LWC1* in Figure 4-1 presents compressibility as a function of gas saturation and porosity. The gas saturation ranges between 0 (fully water bearing) and 1 (fully gas bearing) and the porosity varies between 0.06 (6%, being

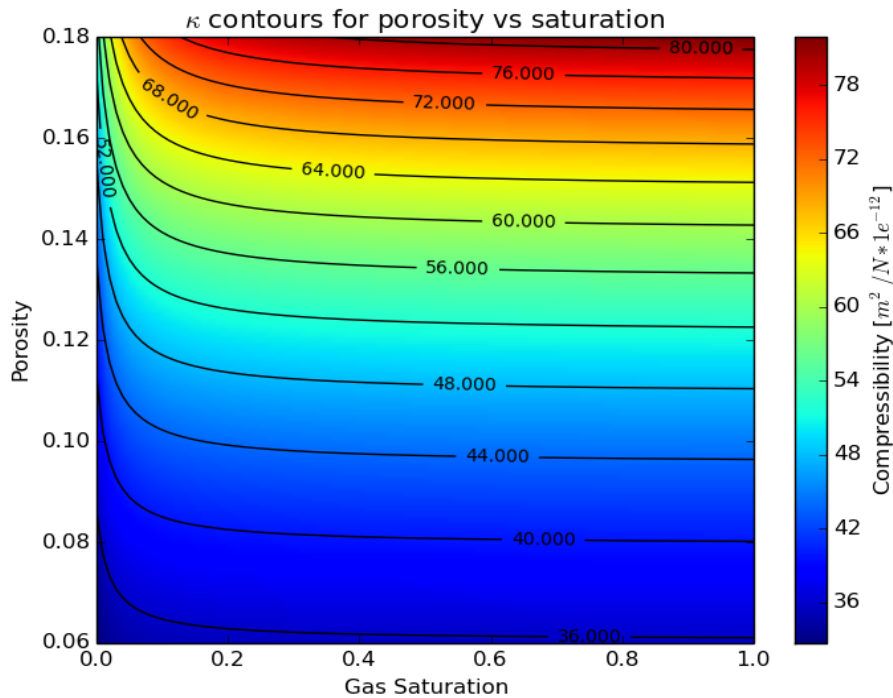


Figure 4-1: Compressibility as a function of the endmember sand porosity and gas saturation, modelled for reservoir *LWC1*, which is calculated to have an average critical porosity of 30%.

typical low-end reservoir cut-off) and 0.18 (18%, maximum porosity observed in well X). The colours represent the compressibility value for each combination of gas saturation and porosity. Additionally, contour lines are plotted to highlight the gas saturation - porosity functions resulting in constant compressibility.

On this plot, it can be seen that compressibility changes much more rapidly in the vertical than in the horizontal direction, therefore indicating again that porosity has a much greater impact on compressibility than gas saturation. The increase of compressibility with porosity is also a non-linear one, as can be seen from the compressibility contours that are moving closer as the porosity becomes larger. Furthermore, in the horizontal direction a steep increase of compressibility with gas saturation is visible up to a gas saturation of approximately 15%, after which the iso-compressibility contours flatten. This effect is more severe for larger porosities. Therefore, it becomes clear from these plots that distinguishing between a 15% and 100% gas filled reservoir based on compressibility alone will be very challenging, especially when the reservoir has a low porosity.

I have to mention however, that my adaptation of the critical concentration model didn't result in a perfect match of the modelled compressibility results with the observed data. In fact, the for the initial sandstone porosity (7.86%) and gas saturation (55%) simulated average compressibility for reservoir *LWC1* is $3.96e^{-11}$, whereas it should be $3.30e^{-11} \text{ m}^2/\text{N}$. Nevertheless, these results still explain the relative effects of porosity versus gas saturation clearly within the assumptions of this simple model.

Part II

Synthetics and Multiple Prediction

Synthetic gathers

During this second stage of my thesis, I have created many synthetic gathers, which provide an idea of the sensitivity of seismic data to saturation and porosity changes. I created these gathers with the Delft Inversion software, Helios, that utilises the Kennett invariant embedding method.

5-1 Kennett invariant embedding method

The Kennett invariant embedding method describes the response of an oblique plane wave incident on a horizontally layered medium [Gisolf and Verschuur, 2010] (see also Figure 5-1);

- by using relationships between the four incident waves (P- and S- waves illuminating the medium from above and from below) and the four transmitted/reflected/converted waves (reflected P- and S-waves and transmitted P- and S-waves);
- as a function of reflection and transmission coefficients (16x), and the extrapolation operator Q ;
- where the extrapolation operator itself is a function of the thickness of the layer d , and the frequency and horizontal slowness of the plane wave;
- where the reflection and transmission coefficients are described by the Zoeppritz equations (and which are a function of the angle of incidence, density, compressional and shear velocity of the different layers).

As noted by [Mavko et al., 2009], the Kennett method involves some assumptions, in part driven by Zoeppritz' boundary conditions, which are that:

- the medium is a horizontally layered medium with no lateral heterogeneities;
- the layers are isotropic linear elastic;
- the wave field is described by a plane wave.

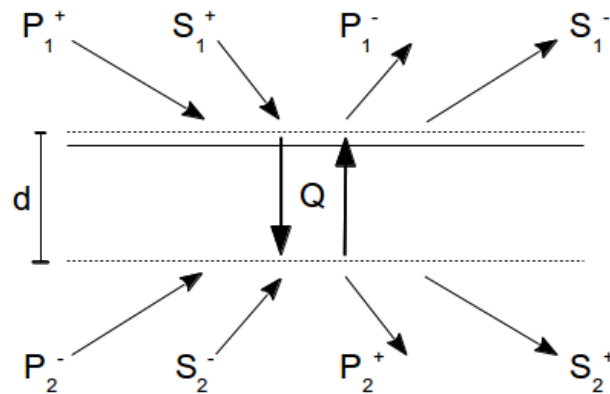


Figure 5-1: Four incident P- and S- waves illuminating a horizontally layered medium from above and below and the four resulting P- and S-waves after reflection, transmission and/or conversion of the incident waves.

5-2 Results

PP synthetic gathers of fluid substituted logs

Synthetic gathers were modelled for the original logs and for the fluid substituted logs, which I had created previously using Gassmann's equations (see Chapter 3), with a 7-12-40-50 Hz bandpass filtered wavelet. Although the Kennett method can compute both PP and PS data, the focus of this thesis will be on the PP-gathers, because only this type of seismic field data will be available for this study. A PP gather is a gather in which the incident wave is a P-wave and the final detected wave is also a P-wave. However, the wave may have experienced mode conversions and/or multiple reflections during its travel path.

In the centre of Figure 5-2, the migrated synthetic PP gather modelled for the original log data over the target interval can be seen. On this figure, a clear decrease of amplitude with slowness can be observed for the blue-red doublet located around 0.065s (indicated by the pink arrow). This doublet is related to reservoir *LWC1*; the low effective porosity (10%), high gas saturation (55%) sandstone reservoir. Furthermore, a move-out for high slowness values is visible for all events. In migrated time you would expect flatness of the event, so this move-out might be due to stretching or, in case of the downward dips, to mode conversions.

The left gather in Figure 5-2 shows the migrated synthetic PP gather modelled for the fluid substituted log data with a target gas saturation of 80% in reservoir *LWC5*. Reservoir *LWC5* originally has a high effective porosity (16%) and a low gas saturation (12%). It can be observed that the second blue loop around 0.085s (indicated by the orange arrow), corresponding to reservoir *LWC5*, has a higher amplitude than on the original migrated synthetic gather and that the decreasing amplitude versus angle (*AVA*) effect for this loop is more visible now. These effects are compared to bounding lithologies best visible on the right gather in Figure 5-2, which shows the difference between the previous two gathers.

In general, I found that an increased gas saturation results in an increased 'softness'¹ of the

¹With the term 'softness' I mean having a lower impedance.

sandstone reservoirs. In Figure 5-3 the migrated synthetic PP gathers for fluid substituted log data with a target gas saturation of 80% (on the left) and of 10% (in the centre) in reservoir *LWC1* can be seen, together with the gather showing the difference between the two (on the right). However, when comparing the difference plots of Figure 5-2 and Figure 5-3, it is obvious that the increased softness with increased gas saturation, is less pronounced for the low-porosity sandstone reservoir. This is in correspondence with the observations made in Chapter 3-2. The differences are overall very subtle though, indicating that it will be hard to distinguish a 10% from a 80% gas saturation, regardless of the type of reservoir.

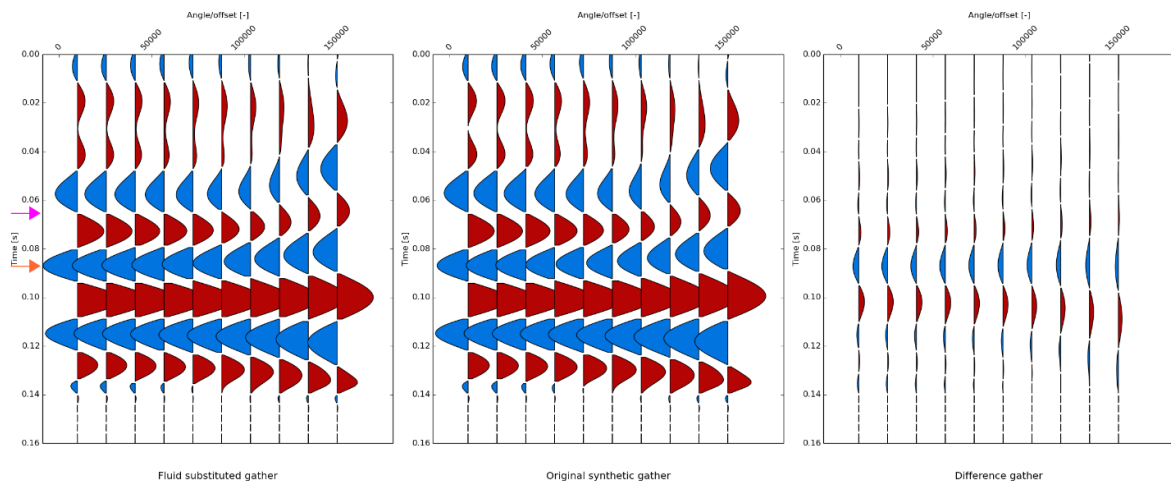


Figure 5-2: Synthetic PP gathers in migrated time over the interval 3510 - 3840m MD, modelled with a 7-12-40-50Hz bandpass filtered wavelet. The left gather is modelled for the fluid substituted log data with a target gas saturation of 80% in reservoir *LWC5* (effective porosity of 16%), the middle gather is modelled for the original log data, where the gas saturation in reservoir *LWC5* is 12%, and the right gather shows the difference between the previous two gathers. The pink arrow indicates the approximate location of reservoir *LWC1* and the orange arrow that of reservoir *LWC5*.

PP synthetic gathers of variable target porosity logs

As a next step, I attempted to create synthetic gathers for sets of logs with variable target porosities within a particular reservoir, while keeping the gas saturation on its original value. This was done in order to observe the effect of an independent porosity increase on the synthetic gathers and to be able to quantify the results of an increasing porosity. No simple physical relationships, like the Gassmann equations for fluid substitution, exist to achieve this goal however.

Initially I attempted to use the critical concentration model, just like before (see Chapter 4-1), but this time running the simulation for each depth sample within the reservoir² and optimising not only for the critical porosity, but also for the shale compressional velocity. Unfortunately this resulted in a too low goodness-of-fit of the for the initial porosity simulated V_p and V_s values with the original V_p and V_s values, from which I concluded that the critical

²Previously I had taken average input values for each reservoir.

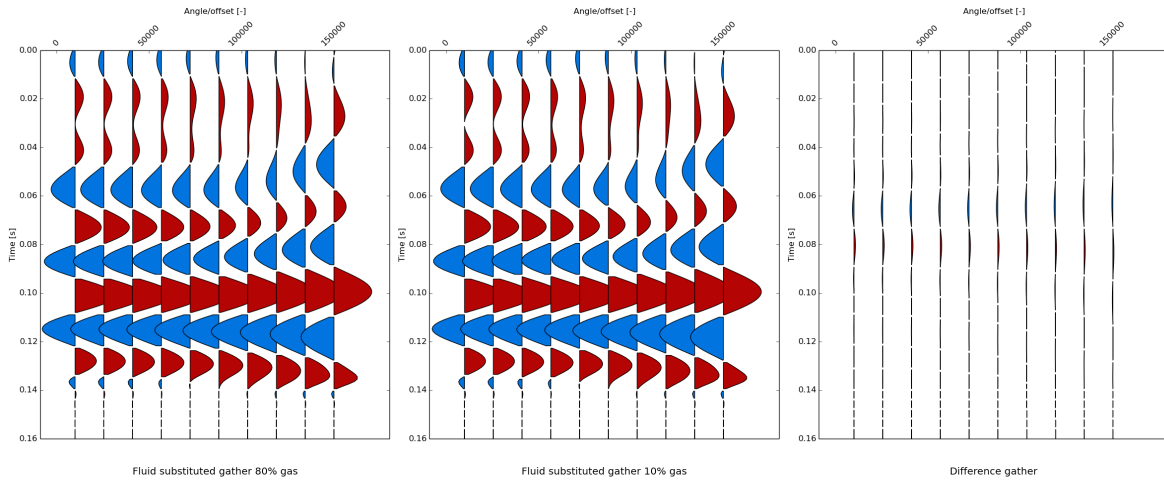


Figure 5-3: Synthetic PP gathers in migrated time over the interval 3510 - 3840m MD, modelled with a 7-12-40-50Hz bandpass filtered wavelet. The left gather is modelled for the fluid substituted log data with a target gas saturation of 80% in reservoir *LWC1* (effective porosity of 9.9%), the middle gather is modelled for the fluid substituted log data with a target gas saturation of 10% in reservoir *LWC1* and the right gather shows the difference between the previous two gathers.

concentration model is not sufficiently accurate to describe these reservoir rocks with. An explanation for the incompatibility of this model could be the unknown shale properties, the bad relation between compressional velocity and density and/or other effects on porosity that are not incorporated in this model, such as cementation.

Eventually, a simple linear regression model was used to model the effect of an independent porosity increase on the synthetic data. For full details, please refer to Appendix B.

As a result, I found that a 30% relative increase in bulk porosity gives an average 6.1% compressibility increase for reservoir *LWC1* and an average 6.8% compressibility increase for reservoir *LWC5*.

In Figure 5-4, the migrated synthetic PP gather modelled for the original log data is now plotted next to the migrated synthetic PP gather modelled for a 30% increased target bulk porosity (compared to the original bulk porosity of 15.5%) in reservoir *LWC5*. It can be observed that the blue loop around 0.085s on the left gather in Figure 5-4 has an even higher amplitude than on the left gather in Figure 5-2 and that the difference gather in Figure 5-4 shows an even larger contrast. This shows that for reservoir *LWC5*, a bulk porosity increase from the original 15.5% to 20.2% has a larger impact on the synthetic data than a gas saturation increase from the original 12% to 80%.

As described in Appendix B, this model assumes that the slope of the linear regression line is representative for the entire reservoir. Unfortunately this is not the case, because each reservoir consists of inhomogeneities, such as an uneven porosity distribution within the reservoir or parts of the reservoir that contain more clay minerals. Thus in order to verify the reliability of this model, I have computed for each reservoir the goodness-of-fit of the regression line with the crossplotted samples, or in statistical terms the coefficient of determination, r^2 . This coefficient of determination ranges from 0 to 1, 1 giving a perfect fit of the regression line. The obtained coefficients can be found in Table 5-1. It can be

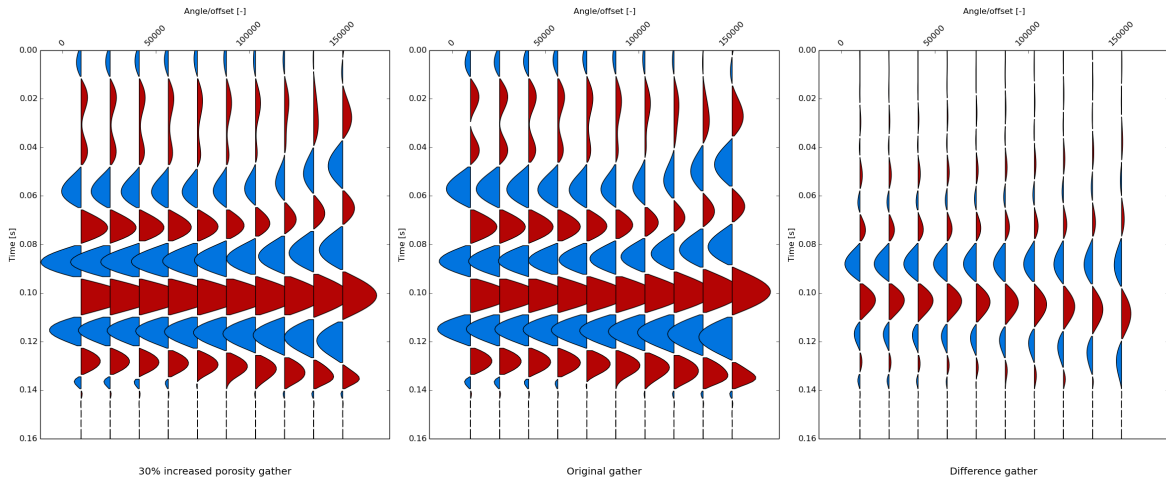


Figure 5-4: Synthetic PP gathers in migrated time over the interval 3510 - 3840m MD, modelled with a 7-12-40-50Hz bandpass filtered wavelet. On the left is the synthetic gather modelled for a 30% increased target bulk porosity (compared to the original bulk porosity) in reservoir *LWC5*, the middle gather is modelled for the original log data and the right gather shows the difference between the previous two gathers.

seen that in case of reservoir *LWC1*, the goodness-of-fit for the crossplot of shear compliance versus compressibility is excellent. However, the goodness-of-fit for the crossplot of shear compliance versus bulk porosity is quite poor. That's why in this case, I decided to calculate shear compliance indirectly via the compressibility - shear compliance relationship. Still, this relationship has a goodness-of-fit that is not perfect, but I found it reliable enough to perform the calculations with.

On the other hand, for reservoir *LWC5*, the goodness-of-fit for the crossplot of compressibility versus bulk porosity is quite poor. So for this reservoir, I decided to calculate compressibility indirectly via the compressibility - shear compliance relationship. One might also wonder why I didn't use the linear regression relationships between bulk porosity, compressional and shear velocity. This is due to the fact that the coefficients of determination for the compressional velocity - bulk porosity and shear velocity - bulk porosity relationships are worse than those for the compressibility - bulk porosity and shear compliance - bulk porosity relationships.

	reservoir	M vs. κ	κ vs. ϕ_{bulk}	M vs. ϕ_{bulk}
r^2	<i>LWC1</i>	0.75	0.53	0.35
	<i>LWC5</i>	0.59	0.35	0.39

Table 5-1: Goodness-of-fit for each crossplot per reservoir.

Chapter 6

Multiple prediction

A multiple is defined as a wave that has been reflected more than once during its travel path. I used the Delft Inversion software, Helios, to see if and where multiples are possibly being generated, as will be described in this chapter. It is important to know this, because multiples generated at shallower depth can obscure events of interest deeper down.

6-1 Multiple theory

Many types of multiple reflections exist in seismic data. Usually they are classified as either short-path or peg-leg multiples, which arrive soon after the primary reflection, or as long-path multiples, which appear as separate events. Most multiple reflections arise from an interface with a strong impedance contrast, such as the water bottom [Yilmaz, 2001].

For the Delft Inversion software it is desirable that all surface related multiples are removed through preprocessing, because this type of multiples is not generated within the reservoir sequence and can therefore not be predicted by the target-oriented inversion scheme [Haffinger, 2013]. Please refer to Chapter 11-2 for a more thorough discussion on this topic.

6-2 Data preparation and approach

After merging the original (shear) sonic and density log curves with the neural network predicted (shear) sonic and density log curves, I could start modelling this log data. As described in Chapter 2-2, log data over the entire interval of the well is needed in order to identify multiple generators and to properly model their multiples using adequate elastic properties.

First of all, I created another set of logs with all properties below a depth of 3600m MD set to a constant value, such that no contrasts would be present over the section containing the reservoirs ¹. For this new set of log data, as well as for the original log data, synthetic gathers

¹This set of log data will be referred to as 'extended overburden' log data.

were created (see Figure 6-1). Apart from this, the total wavefield for both sets of log data was computed at every point in the modelling domain, which is shown in a VSP type display (see Figure 6-2). Finally, an inversion was run for both synthetic gathers, but this will be described later in Chapter 12.

6-3 Results

Synthetic gathers

From the synthetic gathers, I found that internal multiple reflections originating from the overburden are overlaying primary reflections originating from the reservoirs. This can be seen in Figure 6-1, where on the left the synthetic PP gather for the original log data is shown and on the right the synthetic PP gather for the 'extended overburden' log data. Both sets of log data were modelled over the interval 2100 - 3840m MD, thus creating gathers with a length of 800ms. In this figure only the final 250ms of these gathers are shown, corresponding to the target interval approximately. All events below 0.09s on the right gather are the result of multiple reflections and/or mode conversions originating from the overburden (so in this case, everything above 3600m MD). At 0.17s, a multiple reflection is visible for example as a blue negative loop. It is hard to tell exactly where this multiple has been generated however.

In case these multiples are not sufficiently removed during (pre-)processing of the data, they will remain in the data taken into the inversion. Consequently, they could add noise or spurious results to the inversion result. On the other hand, the multiples could be properly accounted for by the inversion, by choosing a limited inversion window.

Virtual VSP displays

In Figure 6-2a, the total wavefield in virtual VSP display for the 'extended overburden' log data, modelled over the interval 2500 - 3840m MD, is shown. Several of its ray-paths have been interpreted on the right of the figure. The green ray-path represents the primary downgoing wavefield, the pink ray-path represents a primary reflected upgoing wavefield that has been reflected at a depth of 2872m MD, the blue ray-path represents a multiply reflected downgoing wavefield that has been reflected at a depth of 3148m MD and subsequently at 2872m MD and finally the orange ray-path represents a multiply reflected upgoing wavefield. This orange wavefield has been interpreted twice, because there are many possible ways this wavefield could have been reflected.

Similarly, the total wavefield in virtual VSP display for the original log data, modelled over the interval 2500 - 3840m MD, is shown in Figure 6-2b. In this figure an interpretation of the up- and downgoing waves can be seen as well. In contrast to Figure 6-2a, the orange ray-path now represents a primary reflected wave, that has been reflected at a depth of 3724m MD. This depth level corresponds to the onset of reservoir *LWC5*. Interestingly enough, the interpreted orange wavefields in Figures 6-2a and 6-2b arrive at exactly the same time (at a depth of 2500m MD), therefore indicating again that a multiply reflected wave is overlaying a primary reflection originating from the target interval.

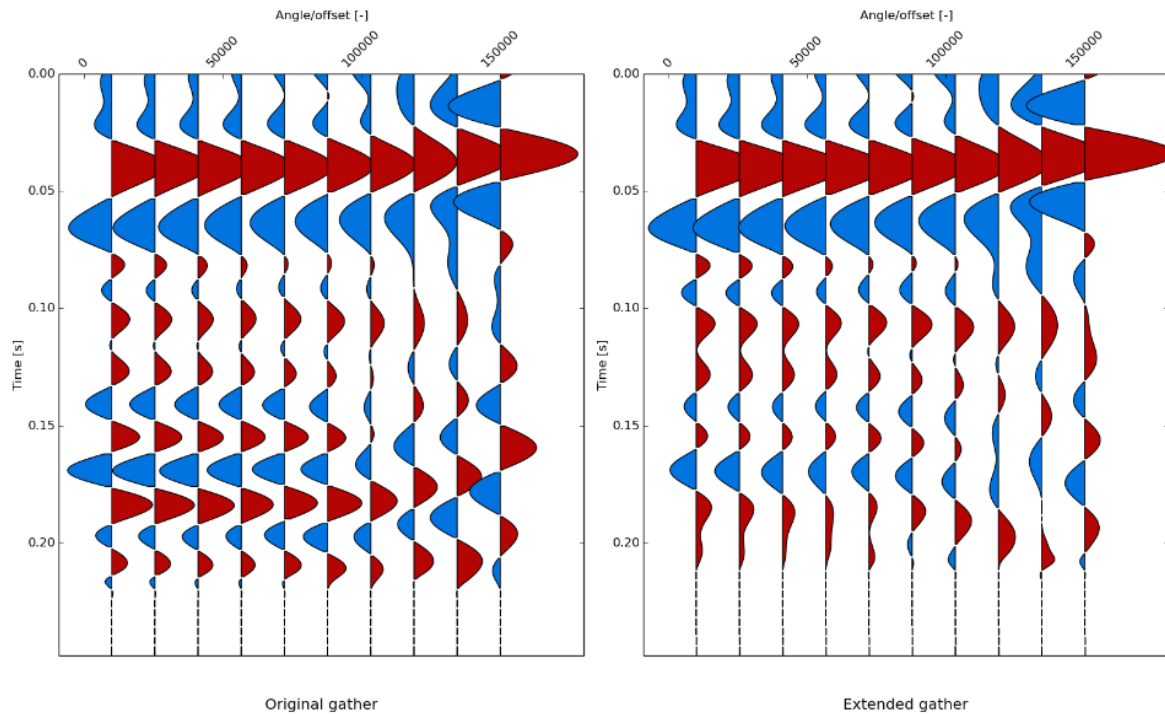
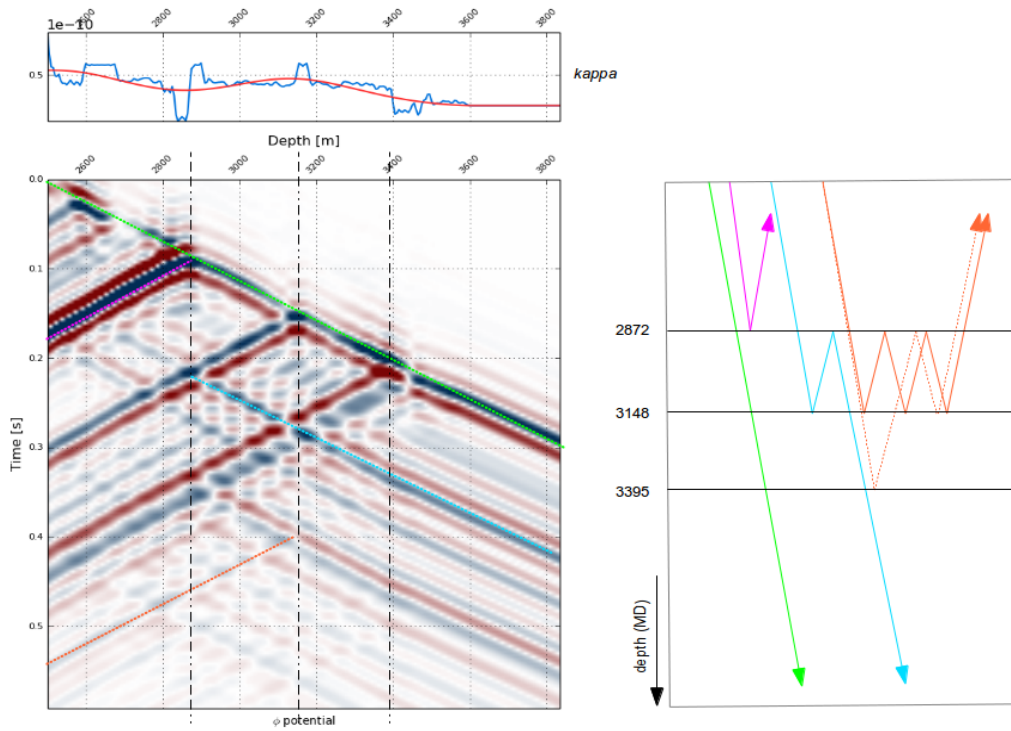
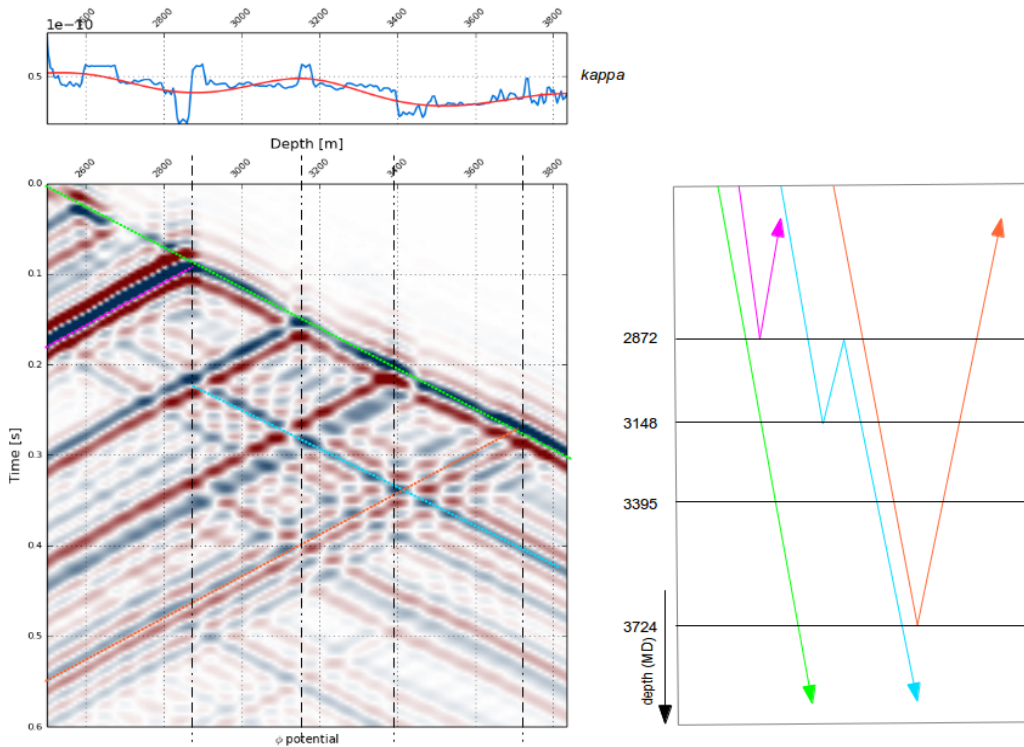


Figure 6-1: The final 250ms of the synthetic PP gathers in migrated time over the interval 2100 - 3840m MD, that were modelled with a 7-12-40-50Hz bandpass filtered wavelet. On the left is the synthetic gather modelled for the original log data and on the right the synthetic gather modelled for the 'extended overburden' log data.

It can be seen that all reflections take place at a depth where there is a large contrast in compressibility. Of course, it has to be kept in mind that in these models, the overburden above a depth of 2100m is not included and that all assumptions made in the Kennett invariant embedding method (see Chapter 5-1) apply to these synthetic results.



(a) The total wavefield in virtual VSP display for the 'extended overburden' log data, modelled over the interval 2500 - 3840m MD, together with an interpretation of several of its up- and downgoing wavefields.



(b) The total wavefield in virtual VSP display for the original log data, modelled over the interval 2500 - 3840m MD, together with an interpretation of several of its up- and downgoing wavefields.

Figure 6-2: The total wavefield for the 'extended overburden' and original log data in virtual VSP display.
 August 19, 2010

Part III

Seismic data and seismic-to-well tie

Chapter 7

VSP data

In the third part of this thesis, the **VSP** and surface seismic data will be described, as well as the seismic-to-well ties of this data with the synthetic data. In this chapter an overview of the **VSP** technique and data will be given.

7-1 VSP technique

The **VSP** technique is a borehole seismic technique, in which either the source or the receivers are placed inside the borehole. In Figure 7-1, an example of a **VSP** survey for an onshore rig is depicted. The **VSP** data are mostly used for correlation with the seismic data and for sonic calibration [Campbell et al., 2005]. One of the major advantages of **VSP** data is that it can be separated into upgoing and downgoing wavefields, thus making interpretation of seismic events easier than on surface seismic data. Apart from this, **VSP** data contains higher frequencies as waves travel only half of the path. Furthermore, a **VSP** can be also used to identify multiples, by stacking the traces within a narrow area following and paralleling the first arrivals [Hampson and Mewhort, 1983]. This stack is known as the corridor stack.

7-2 VSP data

A rig source **VSP** survey was acquired at well X by Baker Atlas in 2006. Measurement levels were recorded between 610 and 3835m **MD**, generally at 10m intervals. The energy source was deployed at an offset of 43m from the wellhead and at a depth of 5m below mean sea level. In general the data quality is considered excellent, but all levels in the section from 2410 to 2720m **MD** were considered unreliable and have thus not been used in the processing. The frequency content of the **VSP** data is approximately 5-120 Hz, with a very low level of random noise.

In Figure 7-2, the corridor stack for this **VSP** dataset is shown, cut out over a time interval, that corresponds to a depth interval of approximately 2100 - 3840m **MD**. Please note that for visualisation purposes, the stacked trace has been copied ten times.

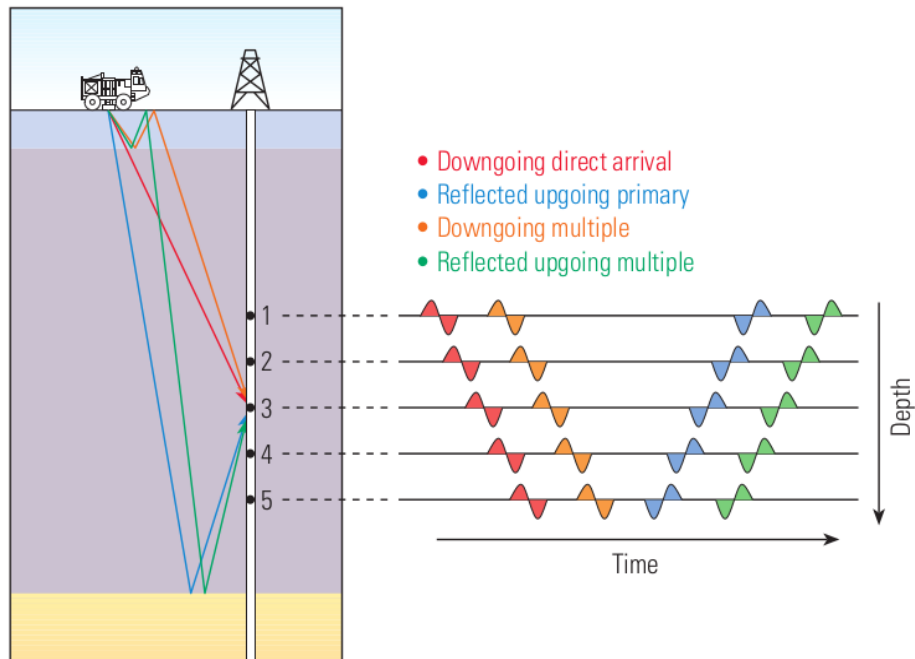


Figure 7-1: A typical onshore VSP survey with the source on the surface and the receivers inside the borehole [Blackburn et al., 2007].

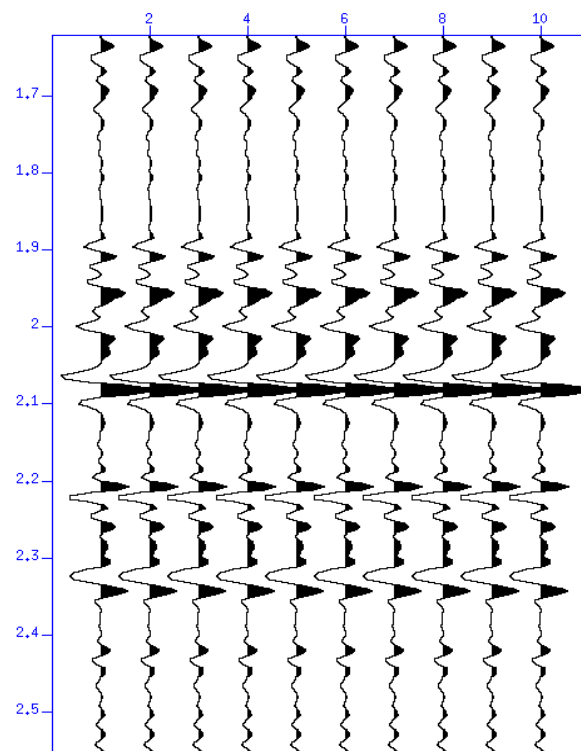


Figure 7-2: VSP corridor stack, limited to a time window of 1700 - 2500 *ms*.

Surface seismic data

The marine surface seismic data used in this thesis were acquired by PGS in 1998. Based on this field data, two datasets have been generated: one post-stack time-migrated dataset and one pre-stack depth-migrated dataset. In this chapter both datasets will be described.

8-1 Post-stack time-migrated seismic data

The seismic data were processed by PGS in 1998, resulting in a stacked data volume. The processing steps include i.a. signature deconvolution, anti alias and f-k filtering, predictive deconvolution, NMO/DMO stacking, pre-migration filtering and Kirchhoff time-migration. So in this case, the available seismic data are already stacked, resulting in a higher signal-to-noise ratio, but on the other hand in a loss of information on the amplitude dependence of reflection coefficients. Furthermore, the seismic post-stack dataset has a sample rate of $4ms$, a trace length of $5000ms$ and a bin size of $25m$ by $25m$. For this study I used a sub-set of the post-stack data that has a dimension of approximately 6.25 square kilometres, covering amongst others the location of well X.

8-2 Pre-stack depth-migrated seismic data

The pre-stack seismic data available to the project were taken from an on-going depth-migration project, at a near-final stage. Therefore, the data did not have all final post-processing applied. The processing steps include i.a. low-cut filtering, noise attenuation, tau-p muting and deconvolution, surface related multiple elimination, anti aliasing, de-ghosting and Kirchhoff pre-stack depth migration. For this dataset, all common offset gathers in the seismic data have been migrated independently without horizontally stacking the traces, therefore preserving the angle-dependent reflectivity information. The seismic pre-stack dataset has a sample rate of $4ms$, a trace length of $4000ms$, a bin size of $25m$ by $25m$ and a maximum offset of $3150m$. For this study I used a sub-set of the pre-stack data that covers an area of approximately 0.49 square kilometres, including the location of well X.

Chapter 9

VSP-to-well tie

Before the VSP data can be inverted, an estimated wavelet from the VSP data is required. This wavelet can be extracted from a seismic-to-well tie of the VSP data with the synthetic data at the well location. Both the underlying theory as well as the results for the VSP-to-well tie will be described in this chapter.

9-1 Seismic-to-well tie technique

A seismic-to-well tie allows the well data, measured in units of depth, to be compared to the seismic data, measured in units of time. First of all, a synthetic gather is generated with the Kennett algorithm from the original well logs using a broadband wavelet (bandpass filtered 0-3-100-120 Hz) and an appropriate slowness range, as was described in Chapter 5. Then, using a least-squares approach, the seismic data are matched to this broadband synthetic gather at the well location, resulting in a gather containing the matched synthetic data, a gather containing the residual (non-matched) data and an extracted wavelet that produces the matched synthetic data if convolved with the well data. These results can be optimised by applying a time shift to the synthetic data, thus aligning events in the synthetic gather with those in the seismic gather. Apart from this, the character of the wavelet can be adjusted, by using a smoothing operator in the frequency domain. The smoother the spectrum of the wavelet, the shorter it becomes in time and the less side-lobes the wavelet has. Finally, the wavelet itself can also be scaled, resulting in a decrease or increase of its amplitude. Scaling the wavelet is done in order to match the amplitudes of the seismic and synthetic gathers.

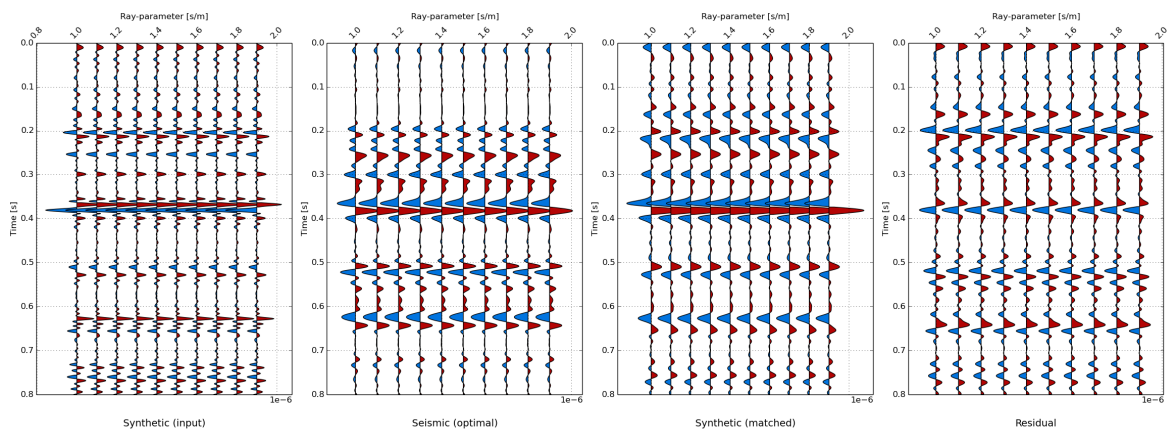
Eventually, a wavelet will be extracted from the most optimal match between the seismic and synthetic data. Ideally, the convolution of this wavelet with the well data would yield the seismic data at the well location. It is very important that this wavelet represents the character of the seismic data correctly, because later on it will be used in the inversion scheme to calculate the incident field (see Chapter 11-2).

9-2 Results

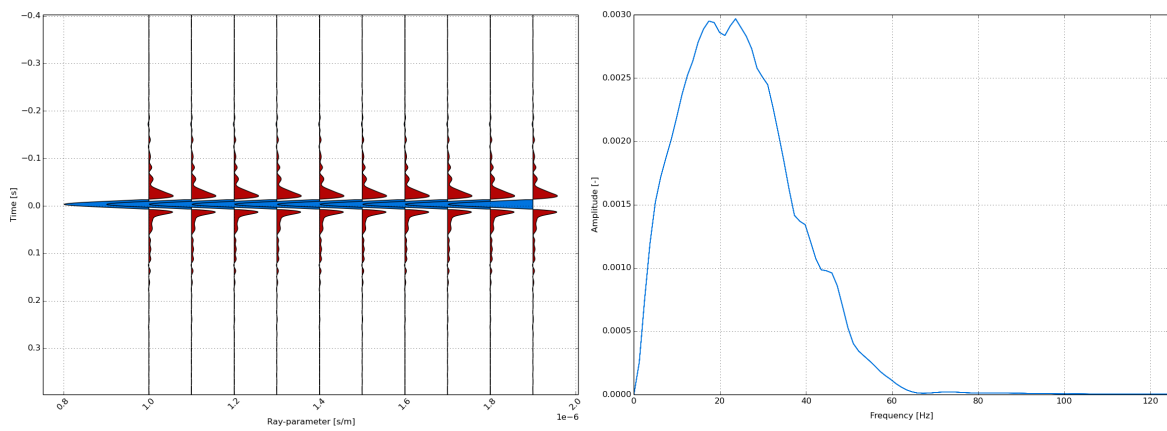
I have performed a seismic-to-well tie of the VSP data with the synthetic data twice: once over the interval 2100 - 3840m MD (Figure 9-1) and once over a smaller interval containing the reservoirs 3300 - 3840m MD (Figure 9-2). I did this in order to see if the extracted wavelet would be very different, which turned out not to be the case, as can be seen when comparing Figures 9-1b and 9-2b.

In Figure 9-1, the results for the seismic-to-well tie of the VSP data with the Kennett synthetic data over the interval 2100 - 3840m MD are shown. It can be observed that the main events present in both gathers match rather well, but that the residual data show some remaining structure (see Figure 9-1a). Some of the residuals may be due to the fact that VSP data are not migrated, and therefore not necessarily on its correct location in case of dipping overburden. However, in this area dips are mild, so this shouldn't have a major impact. The extracted wavelet (Figure 9-1b) is a reverse polarity, almost symmetrical wavelet with a maximum amplitude at time zero and no ringy character. The frequencies present in this wavelet go up to approximately 40 Hz, with a predominant frequency of 24 Hz. The frequency spectrum of the extracted wavelet over the shorter interval (Figure 9-2b) is somewhat narrower and the maximum amplitude of this wavelet is lower.

In Figure 9-2, the results for the seismic-to-well tie of the VSP data with the synthetic data over the interval 3300 - 3840m MD are shown. The time window for these gathers corresponds roughly to the time interval of 0.6 – 0.8s in Figure 9-1a. From this figure, it can be observed that all events in the VSP corridor stack below the high-amplitude event around 0.05s are much lower in amplitude than on the synthetic gather.

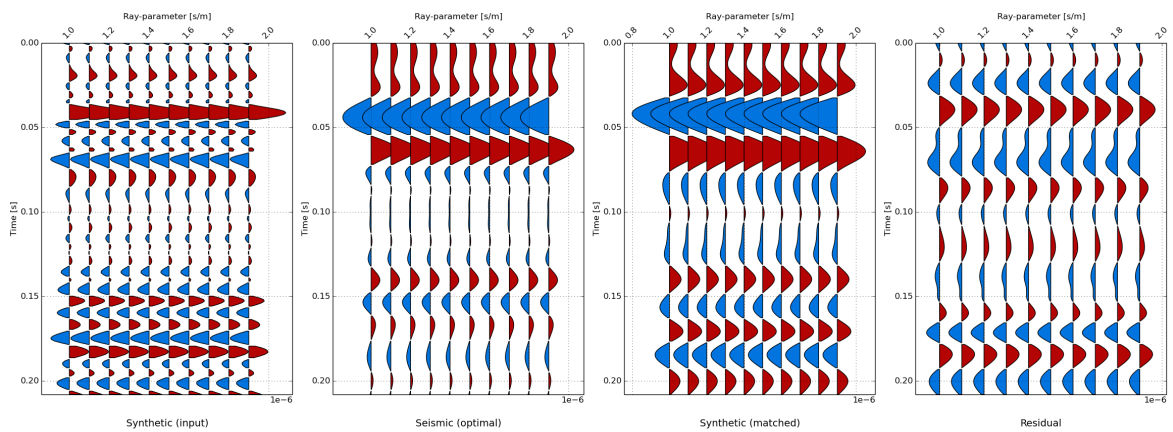


(a) The synthetic gather, VSP corridor stack gather, matched synthetic gather and residual gather.

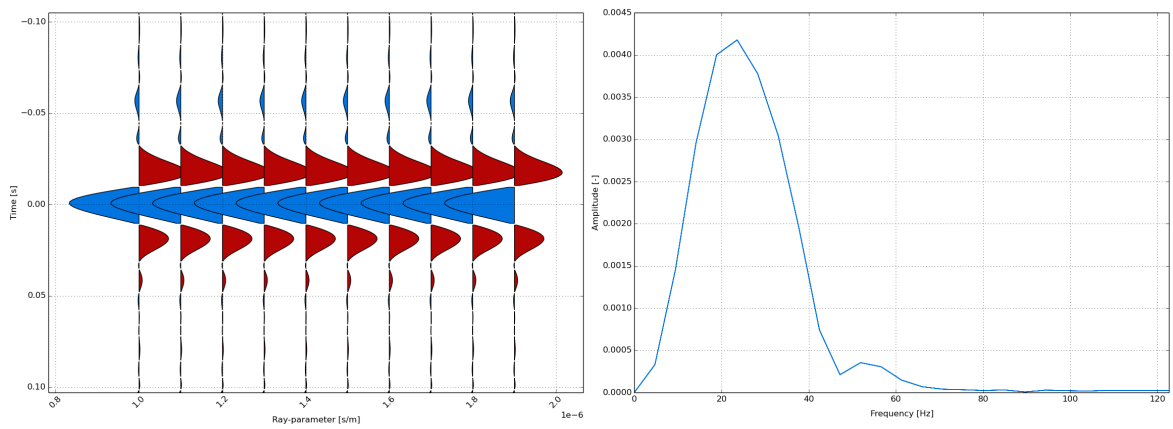


(b) The extracted wavelet estimated from the least-squares match of the original synthetic gather and VSP corridor stack gather.

Figure 9-1: Results for the most optimal seismic-to-well tie of the VSP data with the synthetic data over the interval 2100 - 3840m MD.



(a) The synthetic gather, VSP corridor stack gather, matched synthetic gather and residual gather.



(b) The extracted wavelet estimated from the least-squares match of the original synthetic gather and VSP corridor stack gather.

Figure 9-2: Results for the most optimal seismic-to-well tie of the VSP data with the synthetic data over the interval 3300 - 3840m MD.

Chapter 10

Seismic-to-well tie

Before inversion of the seismic data can take place, an estimated wavelet from the seismic data is required. This wavelet can be extracted from a seismic-to-well tie of the seismic data with the synthetic data at the well location. The technique behind this was already described in Chapter 9-1. The results of the seismic-to-well tie for the post-stack and pre-stack seismic datasets will be presented in this chapter.

10-1 Results

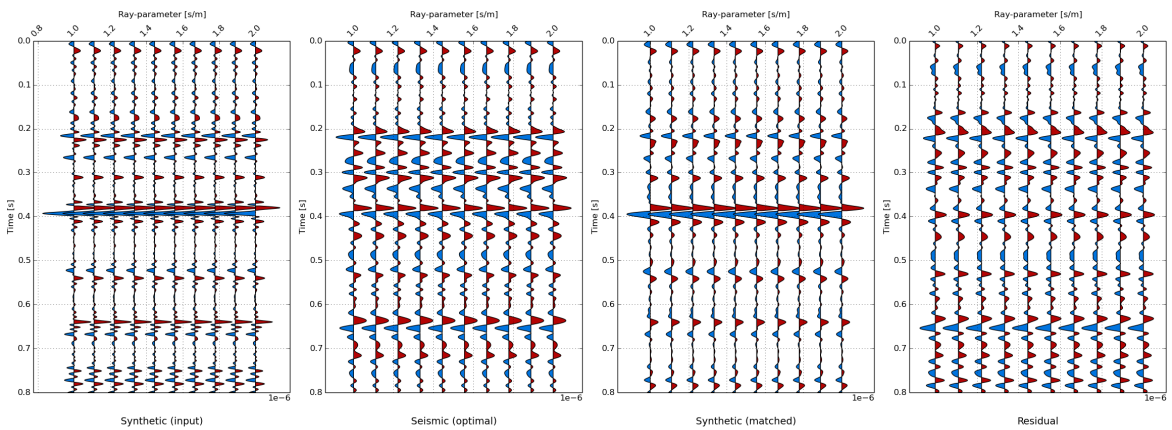
Just like for the VSP data, I have performed a seismic-to-well tie of the seismic data with the synthetic data at the well location twice: once over the interval 2100 - 3840m MD and once over a smaller interval containing the reservoirs 3300 - 3840m MD.

Post-stack time-migrated seismic dataset

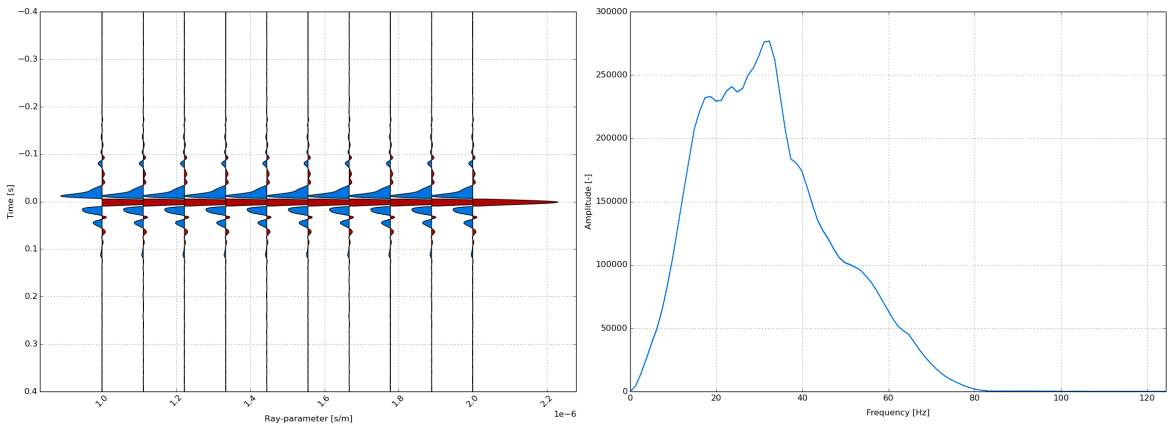
In Figure 10-1, the results for the seismic-to-well tie of the post-stack seismic data with the synthetic data over the interval 2100 - 3840m MD are shown. It can be observed that the main events present in both gathers match reasonably well, but that there are events present in the seismic data that do not occur in the synthetic data, such as the double red loop around 0.7s (see Figure 10-1a). The extracted wavelet in Figure 10-1b is a normal polarity wavelet, that has its maximum amplitude at zero-time, but is rather asymmetric in shape. The frequencies present in this wavelet go up to approximately 50 Hz, with a predominant frequency of 32 Hz. The extracted wavelet over the shorter interval (Figure 10-2b) is rather similar in shape, but has a narrower frequency spectrum and a lower maximum amplitude.

In Figure 10-2, the results for the seismic-to-well tie of the post-stack seismic data with the synthetic data over the interval 3300 - 3840m MD are shown. The time window for these gathers corresponds roughly to the time interval of 0.6 – 0.8s in Figure 10-1a. In this figure, the double red loop that only appears in the post-stack seismic data around 0.1s is even more

visible. From this figure, it can also be observed that the resolution below the high-amplitude event around 0.05s is quite poor.

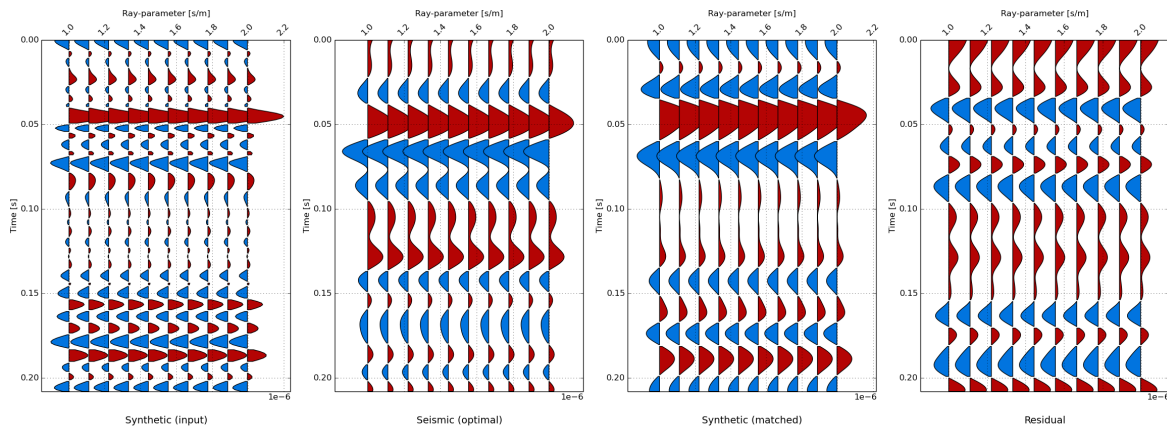


(a) The synthetic gather, seismic post-stack gather, matched synthetic gather and residual gather.

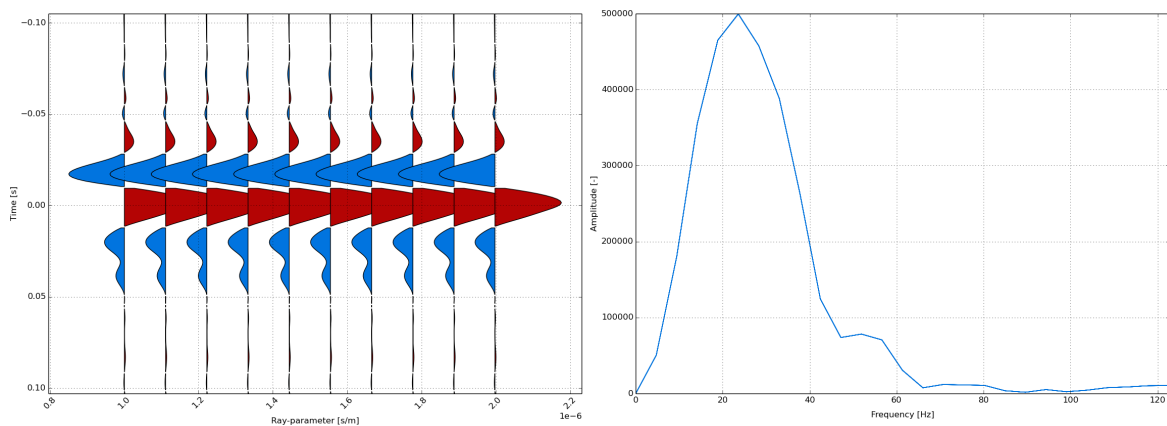


(b) The extracted wavelet estimated from the least-squares match of the original synthetic gather and seismic post-stack gather.

Figure 10-1: Results for the most optimal seismic-to-well tie of the seismic post-stack data with the synthetic data over the interval 2100 - 3840m MD.



(a) The synthetic gather, seismic post-stack gather, matched synthetic gather and residual gather.



(b) The extracted wavelet estimated from the least-squares match of the original synthetic gather and seismic post-stack gather.

Figure 10-2: Results for the most optimal seismic-to-well tie of the seismic post-stack data with the synthetic data over the interval 3300 - 3840m MD.

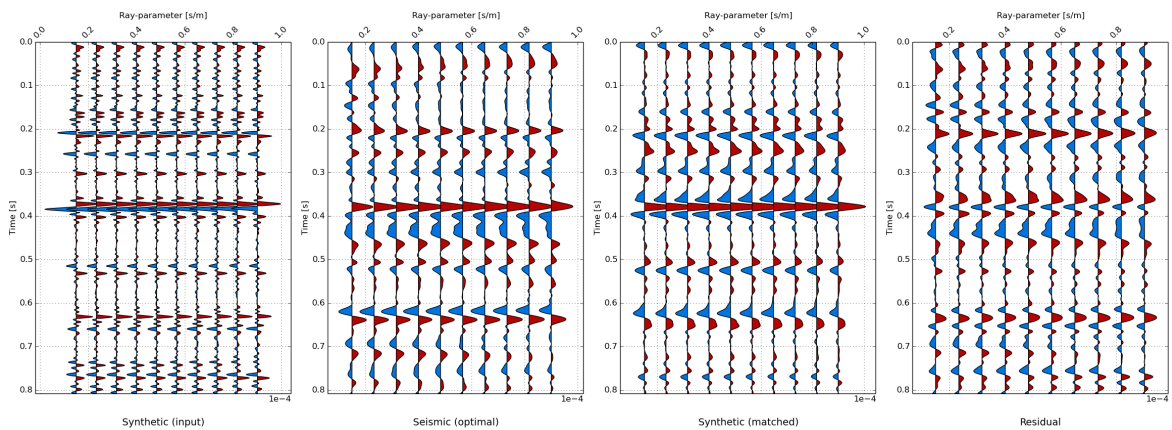
Pre-stack depth-migrated seismic dataset

Before the pre-stack seismic data could be tied to the synthetic data, it had to be converted to the ray-parameter domain. This could easily be done in Helios, where a velocity model is used to convert from the offset to the ray-parameter domain. I created this 2D velocity model from 1D interval velocities, extracted from the well logs, assuming a horizontally layered earth. Considering the well-behaved overburden, this is a fair approximation. Prior to the conversion, a Radon and f-k filter were applied to the pre-stack seismic data in order to remove dipping events on the offset gathers.

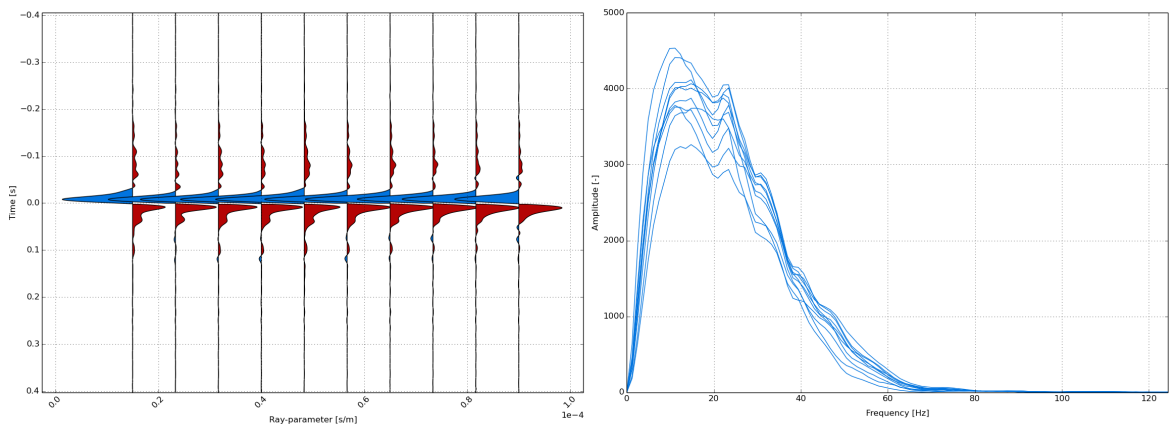
In Figure 10-3, the results for the seismic-to-well tie of the pre-stack seismic data with the synthetic data over the interval 2100 - 3840m MD are shown. Again, all major events in the seismic and synthetic data match rather well, but there are events present in the pre-stack seismic data that do not occur in the synthetic data, such as the blue-red loop around 0.7s (see Figure 10-3a). The extracted wavelet in Figure 10-3b has its energy concentrated in the front of the pulse and is not symmetrical. The frequencies present in this wavelet go up to

approximately 35 Hz, with a predominant frequency of 11 Hz. On the contrary, the wavelet extracted over the shorter interval (Figure 10-4b) is a reverse polarity, almost symmetrical wavelet with a maximum amplitude at time zero. Apart from this, the frequency spectrum of the wavelet is narrower and the maximum amplitude of the wavelet is a bit lower.

In Figure 10-4, the results for the seismic-to-well tie of the pre-stack seismic data with the synthetic data over the interval 3300 - 3840m MD are shown. The time window for these gathers corresponds roughly to the time interval of 0.6 – 0.8s in Figure 10-3a. From this figure, it can be observed that the resolution below the high-amplitude event around 0.05s is very poor.

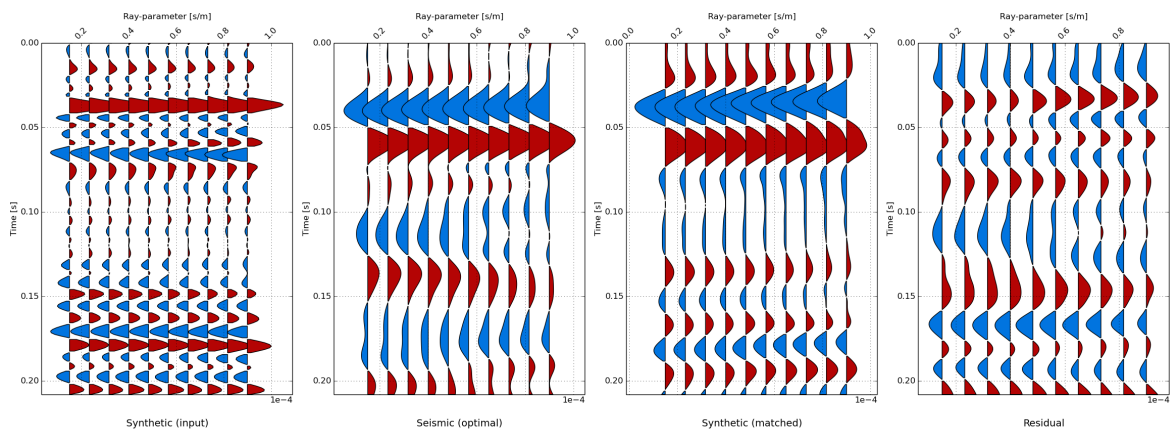


(a) The synthetic gather, seismic pre-stack gather, matched synthetic gather and residual gather.

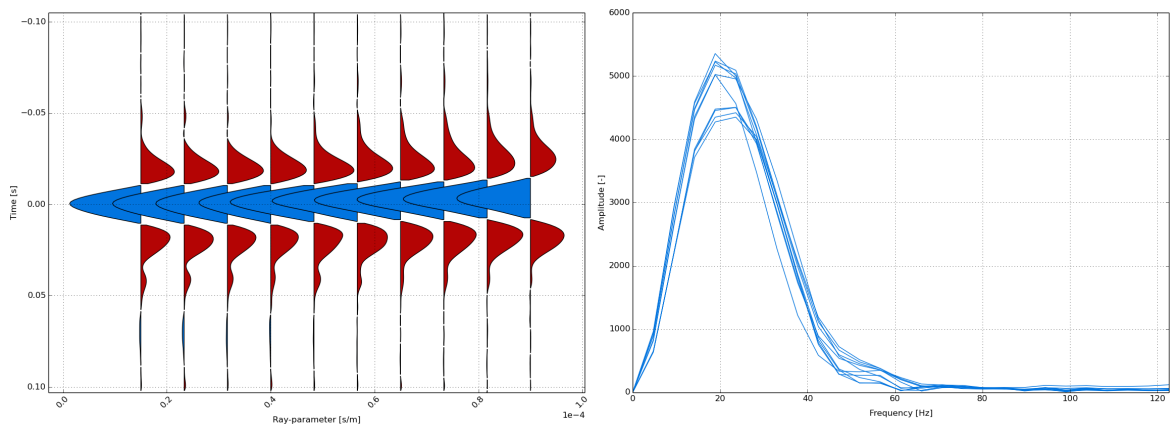


(b) The extracted wavelet estimated from the least-squares match of the original synthetic gather and seismic pre-stack gather.

Figure 10-3: Results for the most optimal seismic-to-well tie of the seismic pre-stack data with the synthetic data over the interval 2100 - 3840m MD.



(a) The synthetic gather, seismic pre-stack gather, matched synthetic gather and residual gather.



(b) The extracted wavelet estimated from the least-squares match of the original synthetic gather and seismic pre-stack gather.

Figure 10-4: Results for the most optimal seismic-to-well tie of the seismic pre-stack data with the synthetic data over the interval 3300 - 3840m MD.

Part IV

Wave-equation based AVO inversion

The inversion algorithm

Seismic data are processed in order to obtain an image of the subsurface. However, this structural image gives no information about the rock properties, whereas these rock properties become increasingly important in the oil and gas industry. This is due to the fact that nowadays very few big discoveries are made and newly discovered reservoirs can be as thin as several meters, therefore requiring high resolution characterisation in order to successfully produce them. Nevertheless, inversion methods can be used to obtain a rock property distribution of the subsurface. In this chapter, inverse theory as well as the inversion algorithm developed by Delft Inversion will be covered.

11-1 Inverse theory

In general each inversion algorithm is based on three main ingredients: the observed data, the unknown material properties and the physical relationships between the data and the unknown material properties. The basic inversion steps are:

- Computing synthetic data from an initial model and by using the forward operator that relates the data and the model space;
- Minimizing the difference between the synthetic and observed data, which leads to a set of equations that are solved to update the medium properties;
- Repeating this process until a satisfactory match between the modelled and observed data is found.

Many different inversion techniques exist, each involving a specific (numerical) solver for the update of the medium properties, certain assumptions regarding the physical relationships and/or a specific set of material properties to invert for. Additionally, many different data types may be available to solve the inverse problem, giving the possibility of running either an independent, joint or coupled inversion.

11-2 The wave-equation based AVO inversion

The inversion algorithm developed by Delft Inversion is an amplitude versus offset (AVO) inversion technique that honours the true non-linear relationship between seismic amplitudes (the observed data) and reservoir properties. Internal multiple scattering, mode conversions and the true travel times over the target interval are all accounted for, because the inversion is based on the full elastic wave-equation. Furthermore, the algorithm inverts directly for compressibility and/or shear compliance, depending on the type of seismic data.

As described by [Haffinger et al., 2016], the algorithm consists of the following steps:

1. Obtaining a first estimate of the reservoir properties through a linear AVO inversion, which is based on the propagation of the wavefield in a smooth, non-scattering background medium. These properties are defined as contrasts against their background values.
2. Using the first estimate of the reservoir properties to update the wavefield. In this step, the non-linear relationship between the measured seismic data and the reservoir properties is built up. This step is based on the scattering integral [Fokkema and van den Berg, 2013]. A higher order of multiple scattering is added in every iteration step.
3. Repeating the AVO inversion, based on the updated wavefield, leading to improved reservoir properties, which are again used to update the wavefield. This iterative procedure is repeated until both the reservoir properties as well as the wavefield don't change any more.

The scheme is illustrated in Figure 11-1. This inversion technique is fundamentally different to other AVO inversion techniques, which are generally based on primary reflections with linearised Zoeppritz coefficients and have the objective to invert for acoustic and shear impedances [Haffinger et al., 2015].

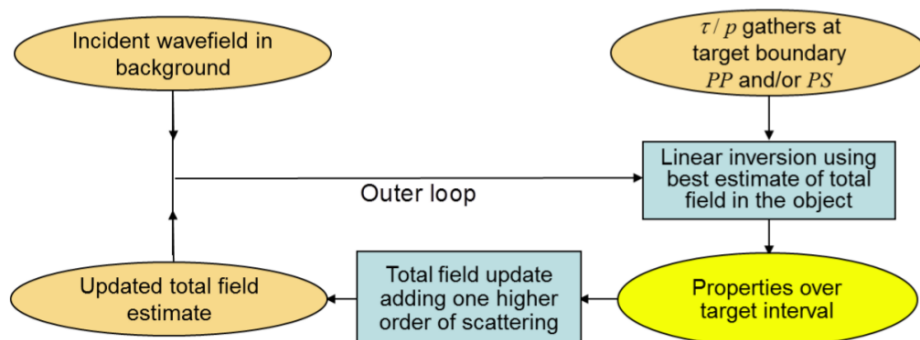


Figure 11-1: A flow diagram describing the non-linear inversion algorithm developed by Delft Inversion [Haffinger et al., 2015].

Chapter 12

Synthetic inversion

With the aim to define boundary conditions for a successful inversion, I inverted synthetic gathers modelled over the target interval. Furthermore, the synthetic gather modelled over the interval 2100 - 3840m MD was inverted, in order to see how the observed multiples in Chapter 6-3 would be explained by the inversion algorithm.

12-1 Results

For synthetic gathers modelled over the interval 3300 - 3840m MD

In Figure 12-1, the inversion results of synthetic gathers, modelled over the target interval 3300 - 3840m MD for the original log data, can be seen. These two gathers were both modelled for a zero-offset slowness range¹, but each with a different wavelet. So the only difference between the inversion result of the synthetic gather on the left (Figure 12-1a) and the inversion result of the synthetic gather on the right (Figure 12-1b) is that the synthetic gather on the left was created with a 7-12-40-50 Hz bandpass filtered wavelet and the synthetic gather on the right was created with a 7-12-60-80 Hz bandpass filtered wavelet.

From this figure it can be observed that the right inversion result resembles the measured response better than the left inversion result, especially over the interval below 3600m MD. This suggests that a higher frequency content in the data is needed to resolve compressibility over the interval containing the reservoirs of interest.

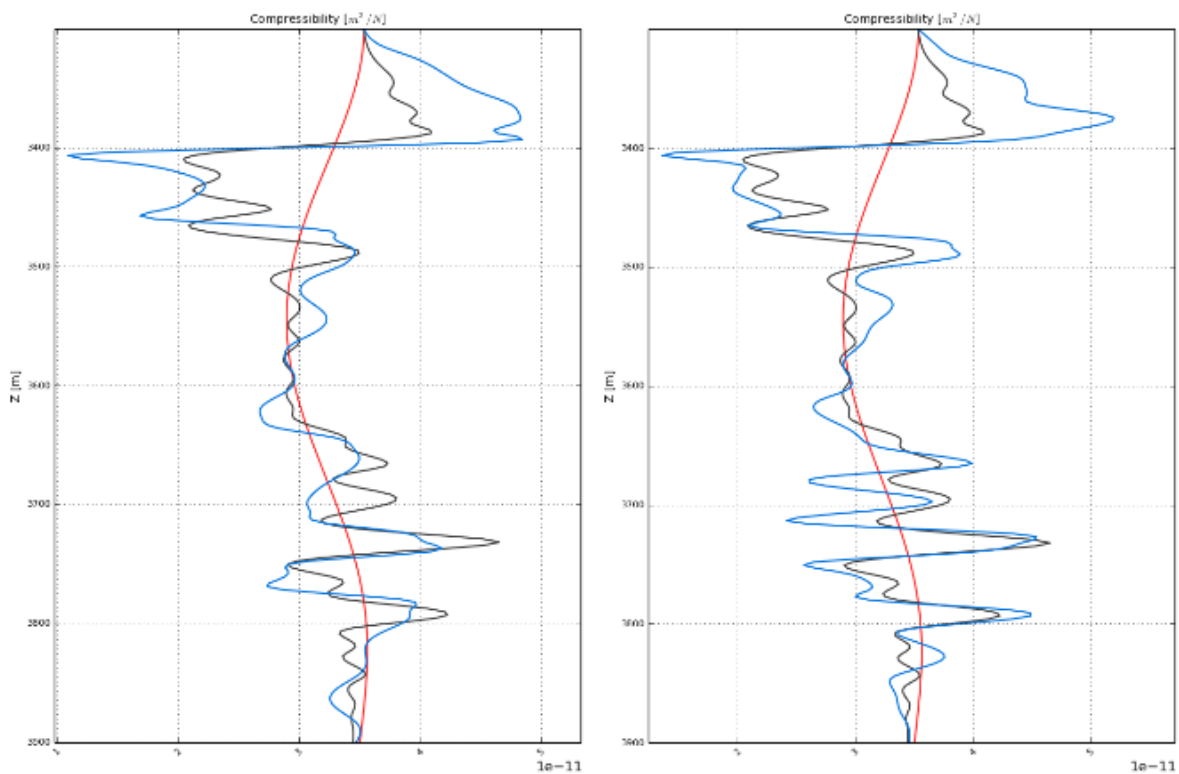
In Figure 12-2, more inversion results of synthetic gathers, modelled over the target interval 3300 - 3840m MD, for the original log data can be seen. In this case, the two gathers were both modelled for a broader slowness range² corresponding approximately to an angle range from 5 – 35°, but again each with a different wavelet. So again the only difference between the inversion result of the synthetic gather on the left (Figure 12-2a) and the inversion result of the synthetic gather on the right (Figure 12-2b) is that the synthetic gather on the left was

¹This was done to resemble the VSP and post-stack seismic data.

²This was done to resemble the pre-stack seismic data.

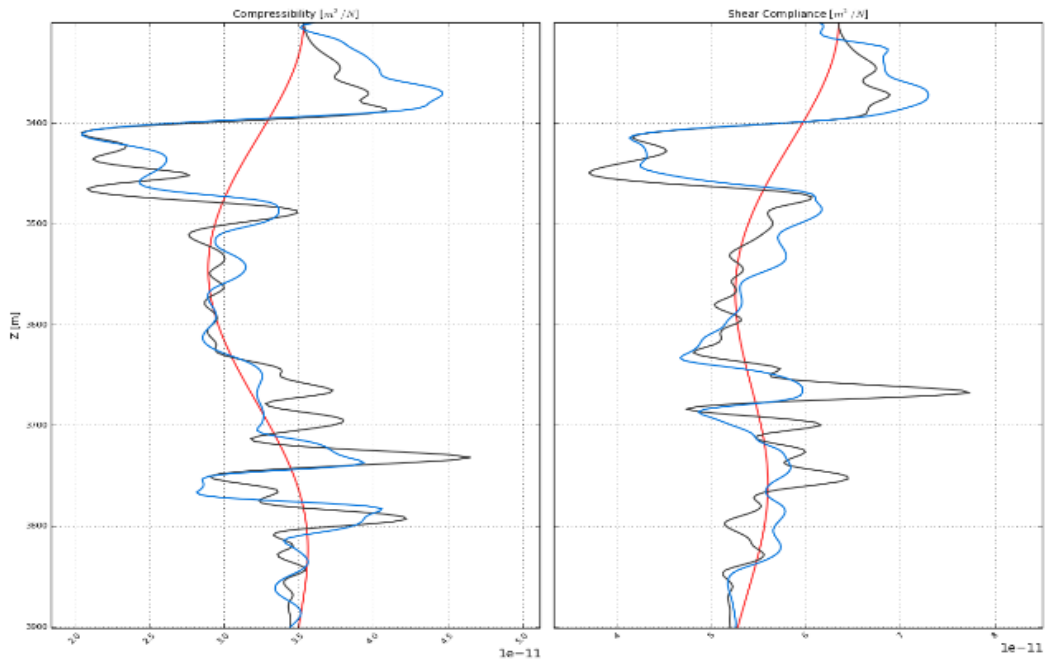
created with a 7-12-40-50 Hz bandpass filtered wavelet and the synthetic gather on the right was created with a 7-12-60-80 Hz bandpass filtered wavelet.

When comparing Figures 12-1a and 12-2b, it can be observed that the inversion result for compressibility in Figure 12-2b now resembles the measured response almost perfectly and that additionally shear compliance can be resolved pretty nicely. This suggests that a wider frequency content as well as higher-angle information are needed to resolve both compressibility and shear compliance over the interval containing the reservoirs of interest. However, Figure 12-2a shows that higher-angle information alone already improves the inversion results significantly. Theoretically this makes sense, because the joint inversion for both compressibility and shear compliance brings more details as the inversion algorithm has more information to converge towards the right solution.

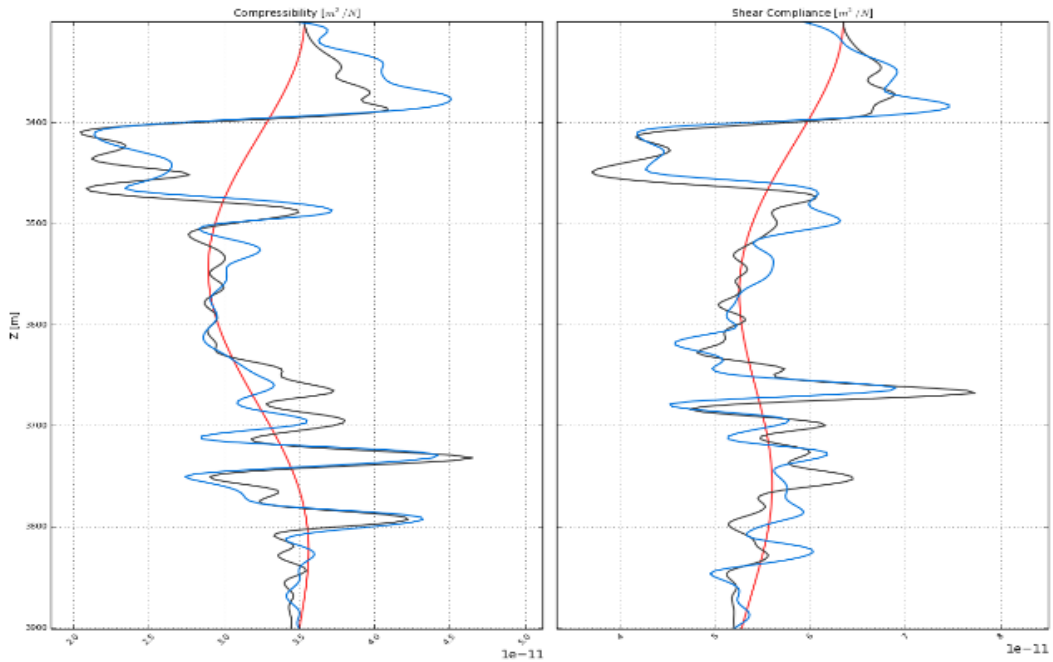


(a) Inversion result for the synthetic gather modelled with a 7-12-40-50 Hz bandpass filtered wavelet. (b) Inversion result for the synthetic gather modelled with a 7-12-60-80 Hz bandpass filtered wavelet.

Figure 12-1: Inversion results (in blue) of compressibility with depth for the synthetic gathers that were modelled for a zero-offset slowness range, but each with a different wavelet, over the interval 3300 - 3840m MD. In black are the original compressibility log curves, which have been anti-alias filtered for 8m sampling.



(a) Inversion results for the synthetic gather modelled with a 7-12-40-50 Hz bandpass filtered wavelet.



(b) Inversion results for the synthetic gather modelled with a 7-12-60-80 Hz bandpass filtered wavelet.

Figure 12-2: Inversion results (in blue) of compressibility and shear compliance with depth, for the synthetic gathers that were modelled for a pre-stack slowness range, but each with a different wavelet, over the interval 3300 - 3840m MD. In black are the original compressibility and shear compliance log curves, which have been anti-alias filtered for 8m sampling.

For synthetic gathers modelled over the interval 2100 - 3840m MD

In Figure 12-3, the inversion result of the synthetic gather, modelled over the interval 2100 - 3840m MD with a 7-12-40-50 Hz bandpass filtered wavelet, for the original log data can be seen. This gather was already displayed on the left panel in Figure 6-1. This synthetic gather was inverted over an inversion window running from 3310 - 3840m MD, in order to obtain only the results over the target interval. Unfortunately, the compressibility contrasts haven't been resolved very well, especially not over the target interval. Therefore, no reliable conclusions with respect to the behaviour of multiples in the inversion algorithm, can be drawn from these results.

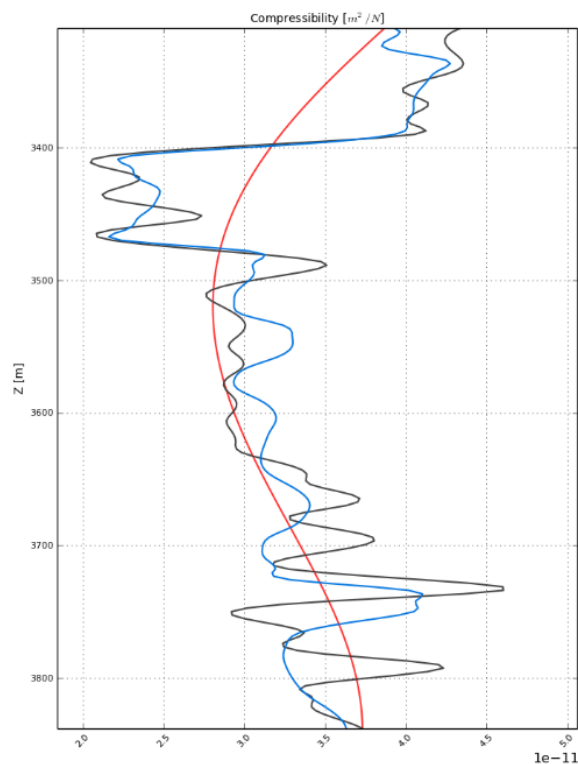


Figure 12-3: Inversion result (in blue) of compressibility with depth for the synthetic gather that was modelled over the interval 2100 - 3840m MD, for the original log data. In black is the original compressibility log curve, which has been anti-alias filtered for 8m sampling.

Chapter 13

VSP inversion

Inversion of the VSP corridor stack was done in order to obtain a multiple-free image of the compressibility distribution at the target interval. In this chapter, the general workflow and results of the VSP inversion will be discussed.

13-1 Data preparation and approach

The VSP inversion was run for the VSP corridor stack, which was cropped to a time window corresponding to the target interval. Further input for the inversion is:

- The extracted wavelet from the VSP-to-well tie (see Figure 9-2b);
- The well log curves of the original log data, which have been anti-alias filtered for 8m sampling. This is done such that the well logs are on approximately the same depth sampling as the seismic data and it depends on the average velocities for the interval and the maximum frequency expected in the data;
- Background log curves, which were created by applying a 4Hz high-cut filter to the original well log data;
- A zero-offset slowness range.

13-2 Results

Figure 13-1 shows the inversion result of compressibility with depth for the VSP corridor stack over the interval 3320 - 3850m MD. It can be seen that the low-compressibility event between 3400 and 3500m MD is well-resolved, as well as the high-compressibility feature at 3725m MD, which corresponds to reservoir *LWC5*. In between, the overall trend as well as some distinct features are picked up by the inversion scheme, although on detailed level, the inversion result deviates from the measured response.

Figure 13-2 shows the VSP corridor stack copied ten times (on the left), the synthetic gather that is the result of iteratively describing the wave-equation as described in Chapter 11-2 (in the middle) and the residual gather (on the right) that shows the difference between the previous two gathers and is magnified by a factor of 2. This figure shows that the data are almost fully explained by the inversion result.

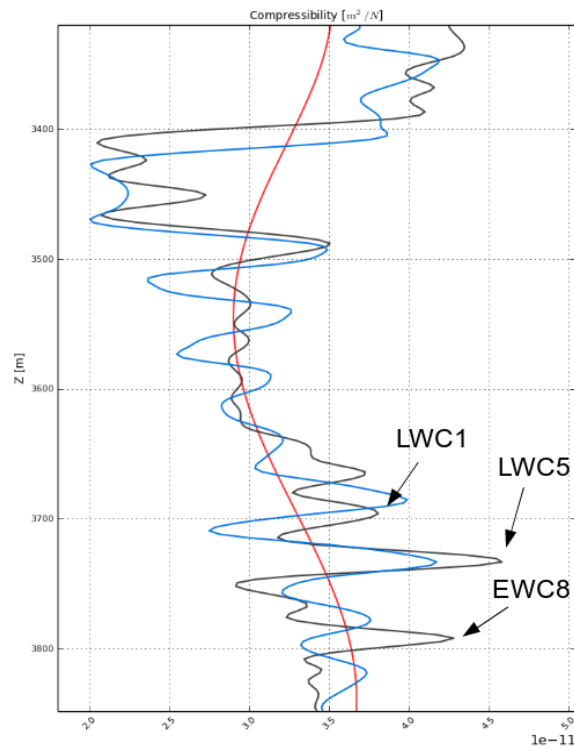


Figure 13-1: Inversion result (in blue) of compressibility with depth for the VSP corridor stack. The blue curve is the inversion result itself, the black curves is the smooth log and the red curve is the background log. The black arrows indicate the approximate locations of three Carboniferous reservoirs.

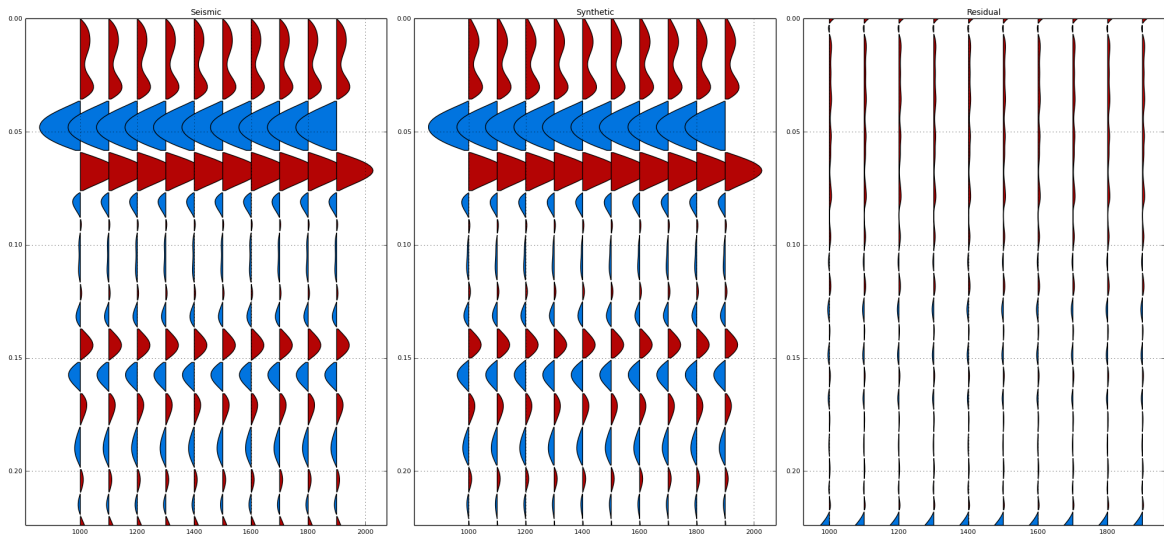


Figure 13-2: The VSP corridor stack (left), the synthetic gather that is the result of convolution of the inversion results with the extracted wavelet (centre) and the residual gather (right) which is magnified by a factor 2.

Surface seismic inversion

In this chapter, the results of the seismic inversion for the post-stack and pre-stack seismic data will be covered in order to obtain an image of the compressibility (and the shear compliance) distribution at the target interval.

14-1 Data preparation and approach

Post-stack time-migrated seismic data

The post-stack seismic data inversion was run for the post-stack seismic data, that was cropped to a time window corresponding to the target interval. The post-stack data was inverted for compressibility only. Further input for the inversion is:

- The extracted wavelet from the seismic-to-well tie (see Figure 10-1b);
- The well log curves of the original log data, which have been anti-alias filtered for 8m sampling. This is done such that the well logs are on approximately the same depth sampling as the seismic data and it depends on the average velocities for the interval and the maximum frequency expected in the data;
- Background log curves, which were created by applying a 4Hz high-cut filter to the original well log data;
- A zero-offset slowness range.

Pre-stack depth-migrated seismic data

Before the pre-stack data could be inverted, it had to be converted to the ray-parameter domain and filtered to remove dipping events. This had already been done for the seismic-to-well tie (see Chapter 10-1) and therefore I continued with that previously edited data-set.

Additionally, a 4-8-45-65 Hz trapezoidal bandpass filter was applied to remove high-frequency noise. Finally, the data-set was cropped to a time window corresponding to the target interval and the pre-stack seismic data was inverted for compressibility and shear compliance. Further input for the inversion is:

- The extracted wavelet from the seismic-to-well tie (see Figure 10-3b);
- The well log curves of the original log data, which have been anti-alias filtered for 8m sampling. This is done such that the well logs are on approximately the same depth sampling as the seismic data and it depends on the average velocities for the interval and the maximum frequency expected in the data;
- Background log curves, which were created by applying a 4Hz high-cut filter to the original well log data;
- A zero-offset slowness range of $1.5e^{-5}$ - $0.9e^{-4}$ s/m, which corresponds approximately to an angle range from 3.9 – 23.2°.

14-2 Results

Inversion of post-stack seismic data

Figure 14-1 shows the inversion result of compressibility with depth for the post-stack seismic data over the interval 3300 - 3900m MD. It can be seen that the low-compressibility event between 3400 and 3500m MD is reasonably well-resolved. Furthermore, the overall trend as well as some distinct features are picked up by the inversion scheme over the interval 3600 - 3800m MD. However, in between, the inversion result deviates clearly from the measured response. Especially the high-compressibility event between 3500 and 3550 m MD is peculiar, because it doesn't show up in the measured response at all. This event is probably related to the double red loop present at 0.12s in the seismic gather (see Figure 14-2), which is not present in the synthetic gather modelled for the original log data, as was already discussed in Chapter 10-1.

Figure 14-2 shows the post-stack seismic data copied ten times (on the left), the synthetic gather that is the result of iteratively describing the wave-equation as described in Chapter 11-2 (in the middle) and the residual gather (on the right) that shows the difference between the previous two gathers and is magnified by a factor of 2. This figure shows that the data are not as fully explained by the inversion result as was the case for the VSP data (see Figure 13-2), but that the data are still well explained.

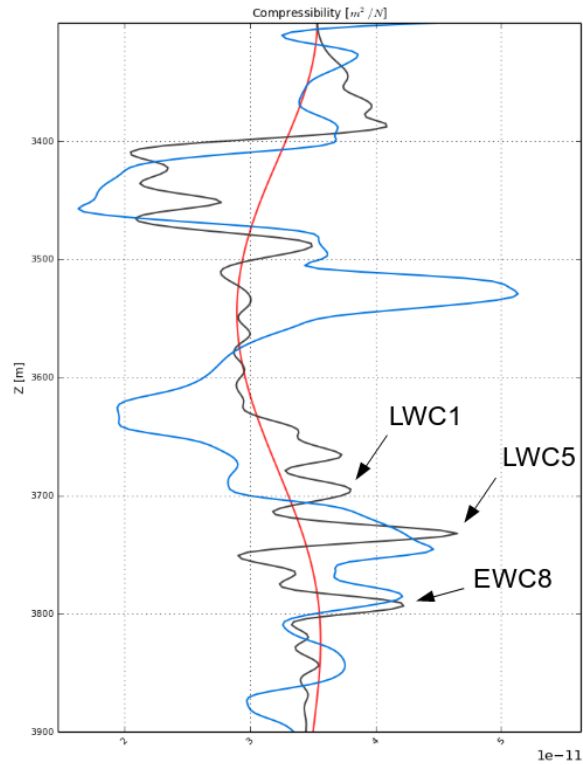


Figure 14-1: Inversion result (in blue) of compressibility with depth for the post-stack seismic data. The blue curve is the inversion result itself, the black curve is the smooth log and the red curve is the background log. The black arrows indicate the approximate locations of three Carboniferous reservoirs.

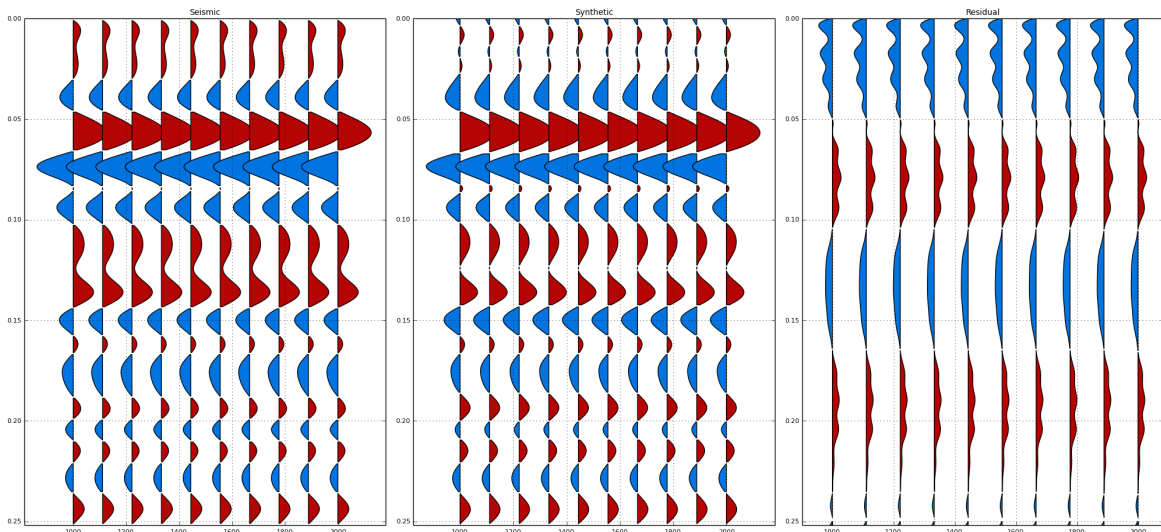


Figure 14-2: The post-stack seismic gather, the synthetic gather that is the result of convolution of the inversion results with the extracted wavelet (centre) and the residual gather (right) which is magnified by a factor 2.

A 3D plot of the compressibility distribution as a result of the post-stack seismic data inversion over the interval 3300 - 3900m MD is displayed in Figure 14-3. In this figure, the 2D cross sections for the inline and crossline that run through the well location are plotted. Thus, the location of the well is at the point where these cross sections intersect. The results of compressibility with depth at this location correspond to the 1D inversion results in Figure 14-1.

It can be seen from this figure, that at least two high-compressibility bodies (indicated by the black arrows) are present in the subsurface. Both bodies are elongated structures that extend laterally for hundreds of meters. Due to their correspondence to the measured response in Figure 14-1 and their high-compressibility values, the upper body is interpreted as the sandstone reservoir *LWC5* and the lower body as the sandstone reservoir *EWC8*.

Depth slices through these high-compressibility bodies are displayed in Figures 14-4a (reservoir *LWC5*) and 14-4b (reservoir *EWC8*). From these figures, it can be seen that both bodies are spread out over a wide area and that the body in Figure 14-4a shows more structure and is more connected than the body in Figure 14-4b, suggesting that this is indeed a sandstone reservoir.

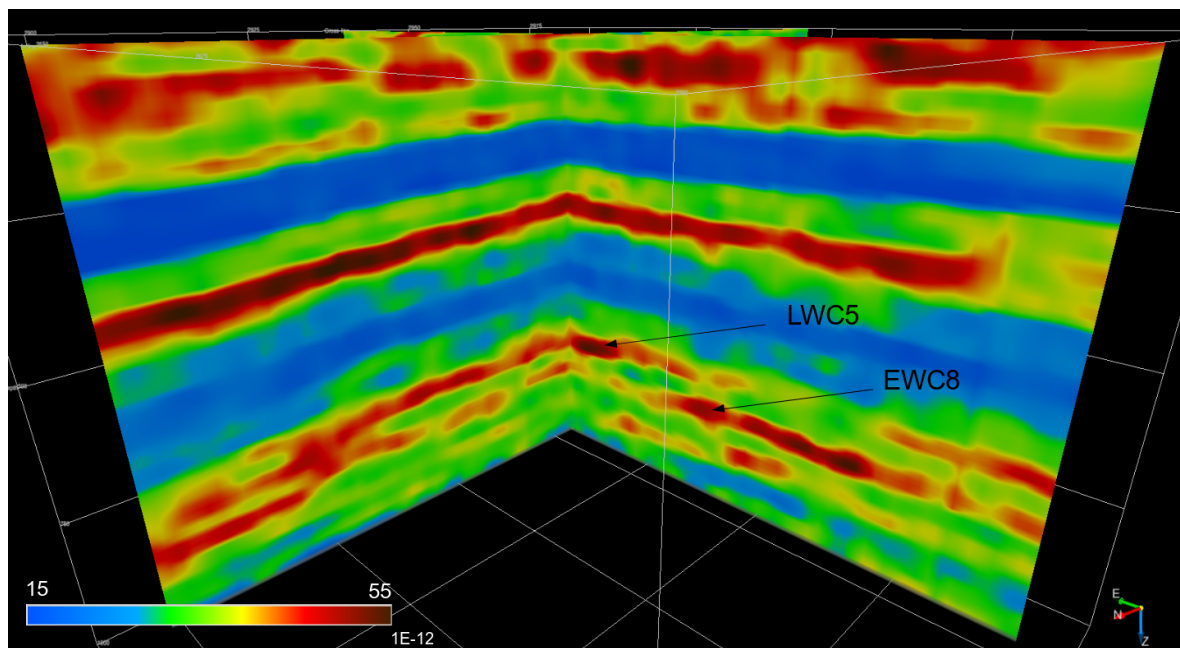
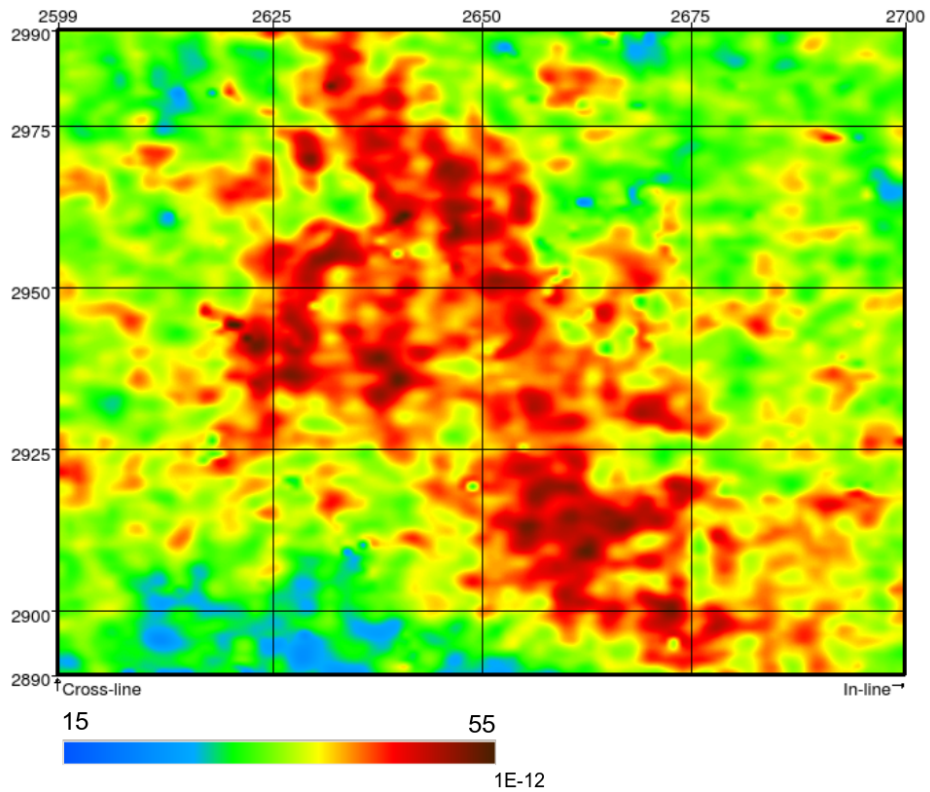
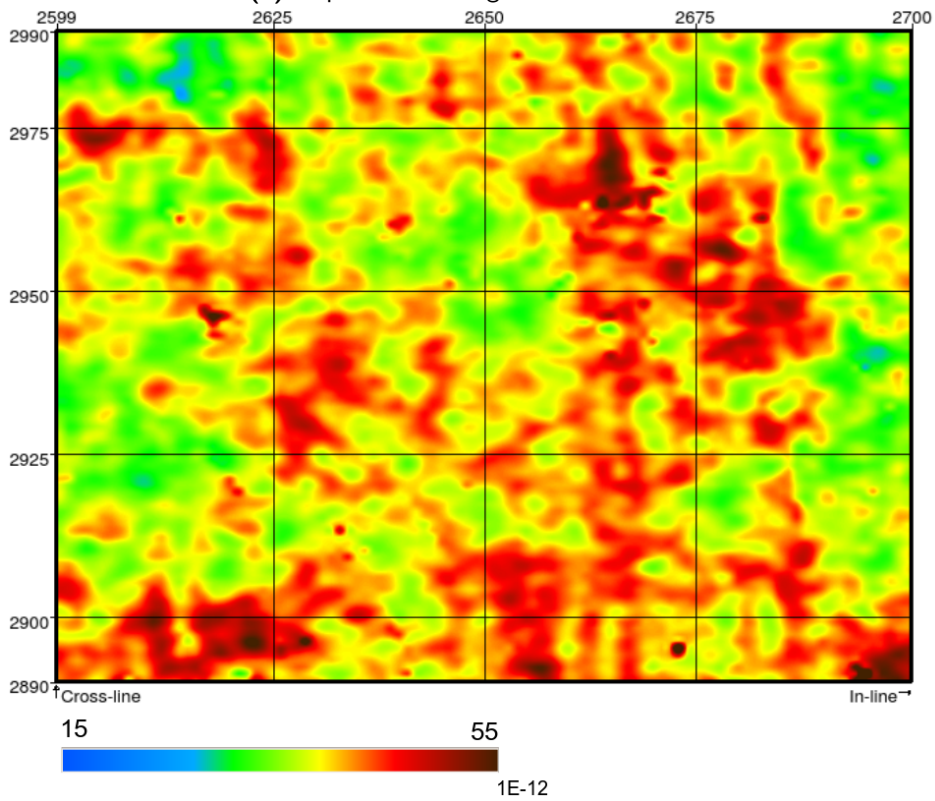


Figure 14-3: 3D plot of the compressibility distribution as a result of the post-stack seismic data inversion over the interval 3300 - 3900m MD. Displayed are the inline and crossline that run through the well location. The reservoirs *LWC5* and *EWC8* are indicated by arrows.



(a) Depth slice through reservoir *LWC5*.



(b) Depth slice through reservoir *EWC8*.

Figure 14-4: Depth slices showing the compressibility distribution as a result of the post-stack seismic data inversion over the interval 3300 - 3900m MD.

Inversion of pre-stack seismic data

Figure 14-5 shows the inversion result of compressibility and shear compliance with depth for the pre-stack seismic data over the interval 3320 - 3850m MD. It can be seen that the low-compressibility event between 3400 and 3500m MD is well-resolved, as well as the high-compressibility feature at 3778m MD, which corresponds to reservoir *EWC8*. In between, the overall compressibility trend as well as some distinct features are picked up by the inversion scheme, although on detailed level, the compressibility inversion result deviates from the measured response. On the other hand, the shear compliance inversion result deviates clearly from the measured response and seems to contain a depth-shift. Perhaps this is due to the somewhat limited angle range in the pre-stack data.

Figure 14-6 shows the pre-stack seismic data (on the left), the synthetic gather that is the result of iteratively describing the wave-equation as described in Chapter 11-2 (in the middle) and the residual gather (on the right) that shows the difference between the previous two gathers and is magnified by a factor of 2. This figure shows that the data are not as fully explained by the inversion result as was the case for the *VSP* data (see Figure 13-2), but that the data are still well explained.

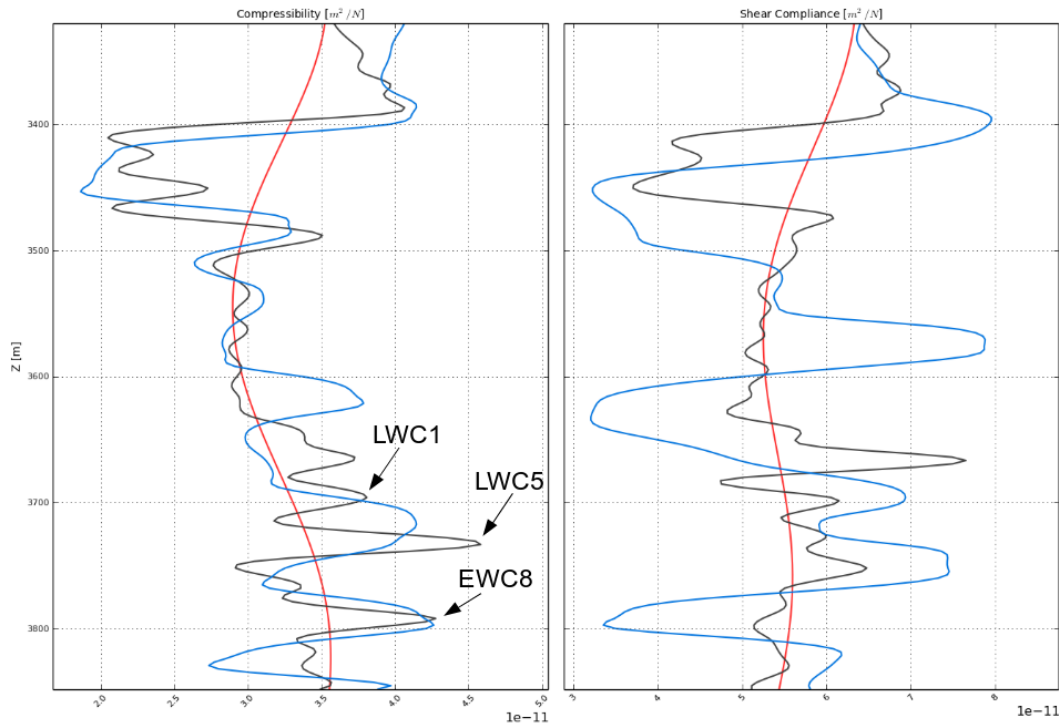


Figure 14-5: Inversion results (in blue) of compressibility and shear compliance with depth for the pre-stack seismic data. The blue curves are the inversion result itself, the black curves are the smooth logs and the red curves are the background logs. The black arrows indicate the approximate locations of three Carboniferous reservoirs.

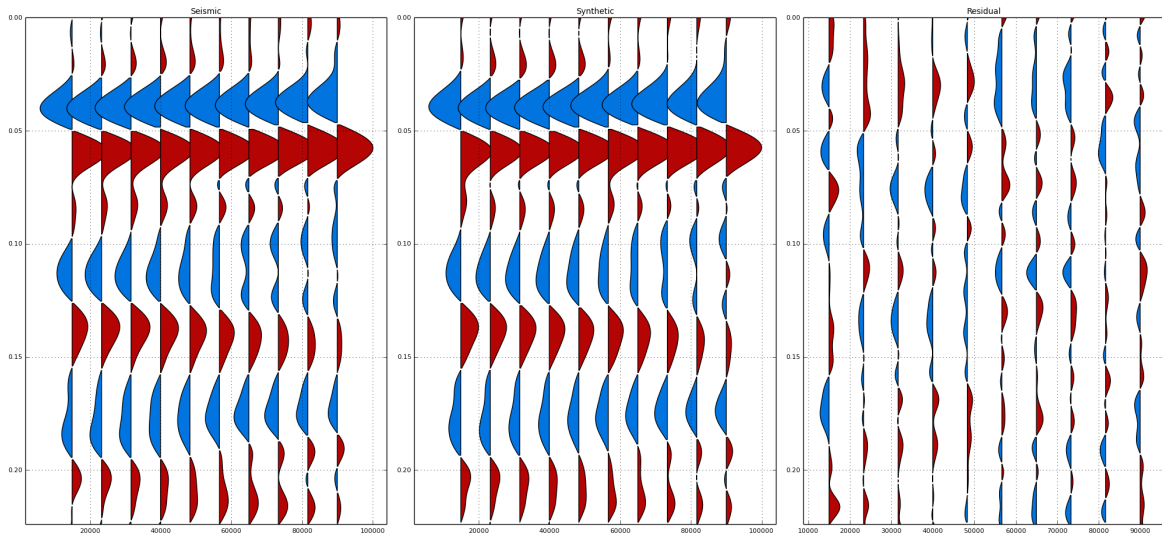


Figure 14-6: The pre-stack seismic gather, the synthetic gather that is the result of convolution of the inversion results with the extracted wavelet (centre) and the residual gather (right) which is magnified by a factor 2.

A 3D plot of the compressibility distribution as a result of the pre-stack seismic data inversion over the interval 3320 - 3850m MD is displayed in Figure 14-7. In this figure, the 2D cross sections for the inline and crossline that run through the well location are plotted. Thus, the location of the well is at the point where these cross sections intersect. The results of compressibility with depth at this location correspond to the 1D inversion results in Figure 14-5. Please note that the lateral extent of the inlines and crosslines is much shorter for the pre-stack data volume than for the post-stack data volume.

It can be seen from this figure, that at least two high-compressibility bodies (indicated by the white arrows) are present in the subsurface. Both bodies are elongated structures that extend laterally. Due to their correspondence to the measured response in Figure 14-5 and their high-compressibility values, the upper body is interpreted as the sandstone reservoir *LWC5* and the lower body as the sandstone reservoir *EWC8*.

Depth slices through these high-compressibility bodies are displayed in Figures 14-8a (reservoir *LWC5*) and 14-8b (reservoir *EWC8*). From these figures, it can be seen that both bodies are spread out laterally, but unfortunately the pre-stack data volume is not sufficiently large to get an idea of the structure of these bodies. However, both high-compressibility bodies do correspond in depth to the high-compressibility bodies observed on the post-stack seismic data inversion results.

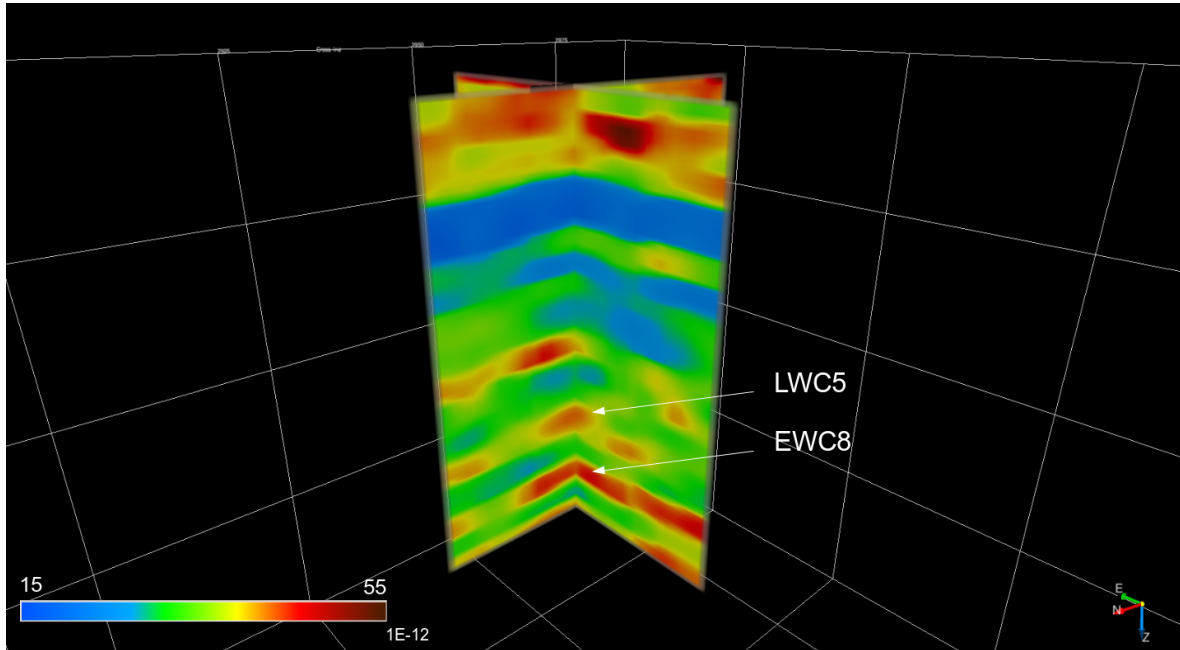
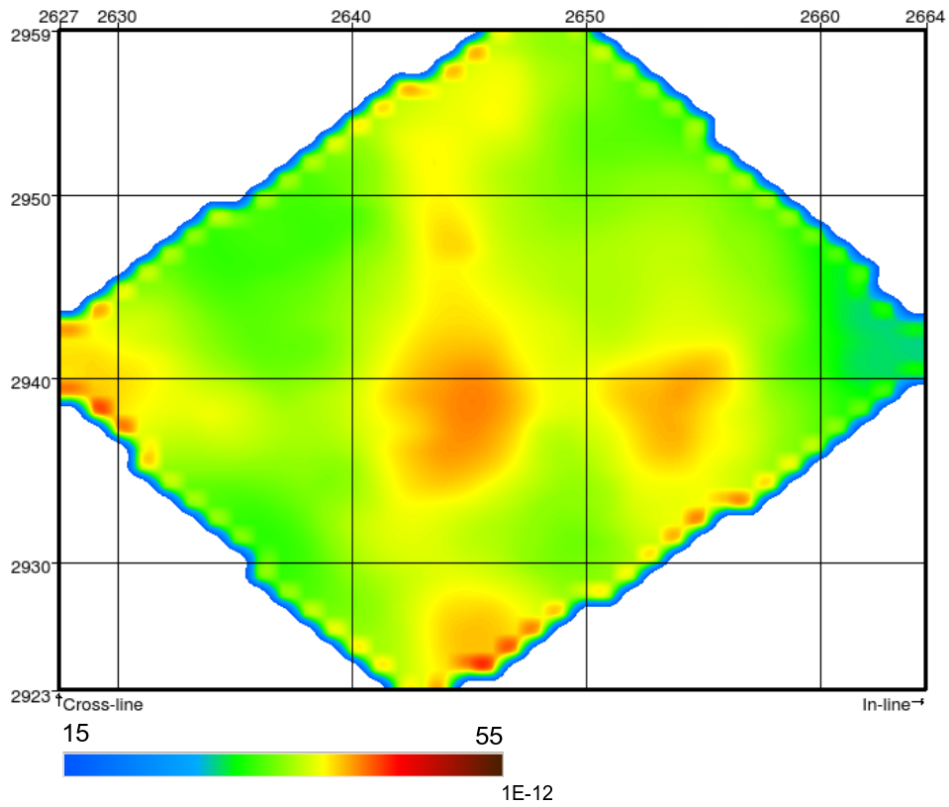
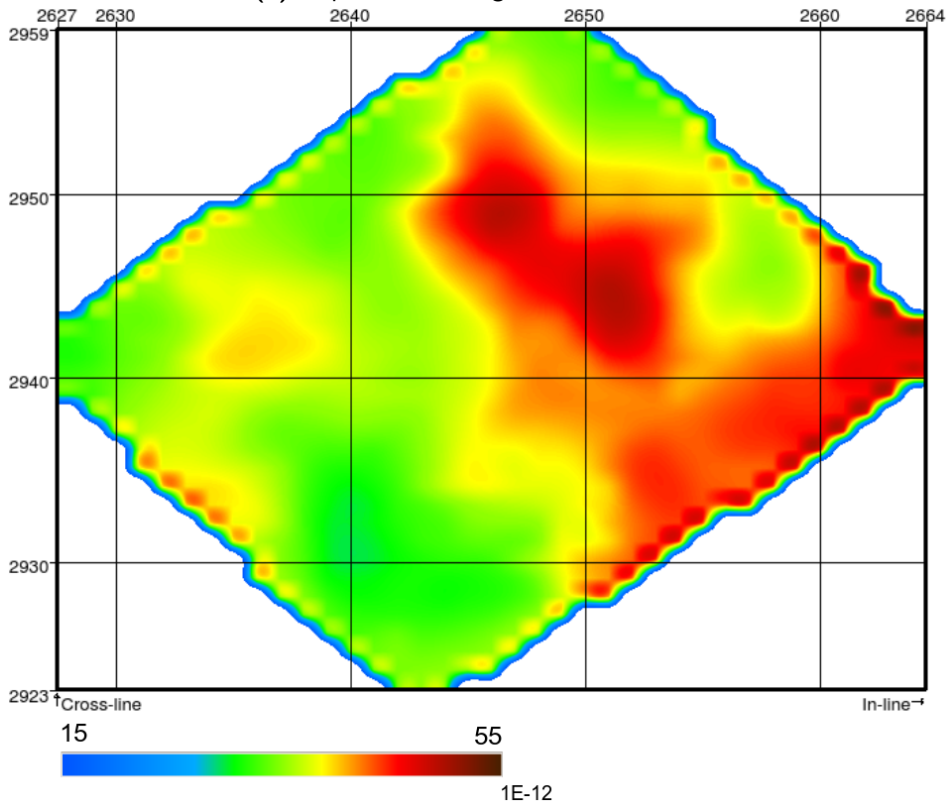


Figure 14-7: 3D plot of the compressibility distribution as a result of the pre-stack seismic data inversion over the interval 3320 - 3850m MD. Displayed are the inline and crossline that run through the well location. Reservoirs *LWC5* and *EWC8* are indicated by arrows.



(a) Depth slice through reservoir *LWC5*.



(b) Depth slice through reservoir *EWC8*.

Figure 14-8: Depth slices showing the compressibility distribution as a result of the pre-stack seismic data inversion over the interval 3320 - 3850m MD. August 19, 2016

Chapter 15

Conclusions

Obtaining high-resolution images of the subsurface in terms of rock properties is a major challenge within the oil and gas industry. Many inversion algorithms have been developed to try and tackle this problem. In this study, the inversion algorithm developed by Delft Inversion is applied to synthetic, [VSP](#) and surface seismic data provided by Wintershall Noordzee. As outcome it has been found that the seismic data quality for this particular data-set is very challenging to provide high-resolution reservoir characterisation. However, many interesting conclusions can be drawn, as presented in this final chapter.

The rock physics analysis showed that compressibility and shear compliance allow for a better discrimination between sands and shales than acoustic impedance and shear impedance. Inverting for compressibility and shear compliance should therefore provide a better discrimination between these lithological classes as well. However, both elastic parameters are needed to do so, compressibility alone would not be sufficient. Furthermore, the rock physics analysis showed that porosity has a greater impact on compressibility than gas saturation. This is very important, because it could lead to a false interpretation of compressibility data derived from seismic: a high-porosity water-saturated reservoir may be falsely interpreted as a commercially attractive reservoir.

Both the rock physics analysis and the synthetic modelling indicate that most impact on the elastic properties is seen when the gas saturation goes from 0 to approximately 10%. This means that it will be very difficult to separate reservoirs containing residual gas from commercially attractive reservoirs on compressibility and shear compliance data.

From the multiple analysis it was found that multiple reflections originating from the overburden are overlaying primary reflections from the Carboniferous reservoirs. The Kennett invariant embedding method proved to be a good method to visualise these multiple reflections.

Seismic-to-well ties have been done for the [VSP](#), post-stack and pre-stack seismic data with the synthetic data at the well location, over both a long interval ranging from 2100 - 3840m [MD](#) and a shorter interval ranging from 3300 - 3840m [MD](#). For each data type, the frequency spectrum of the extracted wavelet over the shorter interval is narrower, indicating that the

data contain less information over this interval. In general, each seismic-to-well tie resulted in a good relative match of the high-amplitude events, but in a rather poor match over the target interval, due to a limited resolution of the seismic data.

The inversion of synthetic gathers showed that data with a broader frequency content give a better inversion result, both for post-stack and pre-stack synthetic data. Additionally, the inversion result of compressibility for pre-stack data is better than that for post-stack data and inversion of pre-stack data allows to resolve shear compliance as well. Thus, in order to obtain good inversion results of both compressibility and shear compliance, pre-stack seismic data with a broad frequency content are needed.

The seismic data don't have the far angle-information and broad frequency content that is needed to accurately resolve these elastic properties, especially not over the target interval. Even though the seismic data quality is not sufficient to provide high-resolution reservoir characterisation, the inversion results do show high compressibility features for the VSP, post-stack and pre-stack seismic inversions. These high-compressibility features could be interpreted as sandstone layers. In fact, the inversion results of compressibility for the VSP and pre-stack seismic data look fairly similar and resemble the measured data at the well location, indicating that these results are quite reliable. On the other hand, I find the post-stack inversion results not so reliable, due to the occurrence of a high-compressibility event that is not present in the synthetic, VSP and pre-stack seismic data. Additionally, the data quality is not sufficient to predict the gas saturation from within these possible sandstone reservoirs.

As a recommendation for further similar studies, I would suggest to invert for a larger data volume in order to have a better estimate of the reliability of the inversion results. Apart from that, I would suggest to invert for a pre-stack data set containing more far-angle information, because this is most probably a limiting factor in this study. Furthermore, data containing higher frequencies should be used in order to obtain high-resolution inversion results for reservoirs at large depths. Finally, more time could be spend to analyse inverted synthetic data, modelled with various types of multiple and converted waves, to see how the inversion algorithm handles multiples in an ideal noise free environment.

Bibliography

- [BHc, 2014] (2014). *The Wireline Services Catalog*. Baker Hughes.
- [Balson et al., 2001] Balson, P., Butcher, B., Holmes, R., Johnson, H., Lewis, M., and Musson, R. (2001). Dti strategic environmental assessment area 2, north sea geology. *British Geological Survey Technical Report, TR/008*.
- [Blackburn et al., 2007] Blackburn, J., Daniels, J., Dingwall, S., Hampden-Smith, G., Leaney, S., Le Calvez, J., Nutt, L., Menkiti, H., Sanchez, A., and Schinelli, M. (2007). Borehole seismic surveys: Beyond the vertical profile. *Oilfield Review*, 19(3):20–35.
- [Campbell et al., 2005] Campbell, A., Fryer, A., and Wakeman, S. (2005). Vertical seismic profiles more than just a corridor stack. *The Leading Edge*, 24(7):694–697.
- [Chen and Eriksen, 1991] Chen, S. and Eriksen, E. (1991). Compressional and shear-wave logging in open and cased holes using a multipole tool. *Geophysics*, 56(4):550–557.
- [Fokkema and van den Berg, 2013] Fokkema, J. T. and van den Berg, P. M. (2013). *Seismic applications of acoustic reciprocity*. Elsevier.
- [Gisolf and van den Berg, 2012] Gisolf, A. and van den Berg, P. (2012). Target-oriented elastic full wave form inversion. In *74th EAGE Conference and Exhibition incorporating EUROPEC 2012*.
- [Gisolf and Verschuur, 2010] Gisolf, D. and Verschuur, E. (2010). *The principles of quantitative acoustical imaging*.
- [Haffinger et al., 2016] Haffinger, P., Eyvazi, F. J., Steeghs, T., Doulgeris, P., and Gisolf, A. (2016). Quantitative prediction of injected co2 at sleipner using wave-equation based avo. In *78th EAGE Conference and Exhibition 2016*.
- [Haffinger et al., 2015] Haffinger, P., von Wussow, P., Doulgeris, P., Henke, C., and Gisolf, A. (2015). Reservoir delineation by applying a nonlinear avo technique—a case study in the Nile delta. In *77th EAGE Conference and Exhibition 2015*.

- [Haffinger, 2013] Haffinger, P. R. (2013). *Seismic broadband full waveform inversion by shot/receiver refocusing*. TU Delft, Delft University of Technology.
- [Hampson and Mewhort, 1983] Hampson, D. and Mewhort, L. (1983). Using a vertical seismic profile to investigate a multiple problem in western canada. *Canadian Journal of Exploration Geophysics*, 19(1):16–33.
- [Kumar, 2006] Kumar, D. (2006). A tutorial on gassmann fluid substitution: formulation, algorithm and matlab code. *matrix*, 2:1.
- [Mavko et al., 2009] Mavko, G., Mukerji, T., and Dvorkin, J. (2009). *The rock physics handbook: Tools for seismic analysis of porous media*. Cambridge university press.
- [Russell and Hampson, 2006] Russell, B. and Hampson, D. (2006). The old and the new in seismic inversion. *CSEG Recorder*, 31(10):5–11.
- [Waterman, 1947] Waterman, J. C. (1947). Geophysical history of the ten section oil field, kern county, california. *Geophysics*, 12(3):402–405.
- [Yilmaz, 2001] Yilmaz, Ö. (2001). *Seismic data analysis*, volume 1. Society of exploration geophysicists Tulsa.

Appendix A

Critical concentration model

The steps used in the critical concentration model are the following.

1. First of all the porosity of the end-member sand is calculated:

$$\phi = \frac{\rho_s - \rho_b + V_{sh}(\rho_{sh} - \rho_s)}{\rho_s - \rho_{fl} + V_{sh}(\rho_{fl} - \rho_s)} \quad (\text{A-1})$$

where:

- ρ_b is the bulk density obtained from the bulk density log
- ρ_s is the density of quartz
- ρ_{sh} is the shale density
- ρ_{fl} is the fluid density:

$$\rho_{fl} = \rho_{HC} \cdot S_{HC} + \rho_w(1 - S_{HC}) \quad (\text{A-2})$$

where ρ_{HC} and ρ_w are the hydrocarbon and brine density respectively and S_{HC} is the hydrocarbon saturation.

- V_{sh} is the shale volume:

$$V_{sh} = \frac{GR - GR_{min}}{GR_{max} - GR_{min}} \quad (\text{A-3})$$

where GR , GR_{min} and GR_{max} are the gamma-ray values for the target interval, the pure sandstone and the pure shale respectively.

2. Then the bulk modulus and shear modulus are calculated from the previously calculated sandstone porosity, the shale moduli, sandstone moduli, shale volume and for a range of critical porosities (ϕ_c):

$$\frac{1}{K_b} = \frac{V_{sh}}{K_{sh}} + (1 - V_{sh}) \frac{1}{K_{sst}} = \frac{V_{sh}}{K_{sh}} + (1 - V_{sh}) \left(\frac{1 - \beta + \phi \cdot \alpha}{K_s(1 - \beta + \phi \cdot \beta \cdot \alpha)} \right) \quad (\text{A-4})$$

where:

- K_s is the bulk modulus of quartz
- K_{sh} is the bulk modulus of shale, calculated from ρ_{sh} , $v_{p_{sh}}$ and $v_{s_{sh}}$
- α is a constant:

$$\alpha = \frac{K_s}{K_{fl}} - 1$$

- β is a constant:

$$\beta = \frac{1 - \frac{\phi}{\phi_c}}{1 + \frac{3}{4\eta_s} \frac{\phi}{\phi_c}}$$

where

$$\eta_s = \frac{\mu_s}{K_s}$$

Similar equations hold for the shear modulus.

3. Thirdly the bulk compressional and shear velocity are calculated from the in step two calculated bulk modulus and shear modulus.
4. The optimal critical porosity is determined by minimizing the least squares error:

$$F = \sqrt{(v_{p_b} - v_{p_{ctl}})^2 + (v_{s_b} - v_{s_{ctl}})^2} \quad (\text{A-5})$$

Where v_{p_b} and v_{s_b} are the previously calculated compressional and shear velocity of the fluid filled rock and $v_{p_{ctl}}$ and $v_{s_{ctl}}$ are the control compressional and shear velocity derived from the log data. The smallest value for F thus corresponds to a critical porosity value that is characteristic for this reservoir.

5. Finally, the bulk modulus and shear modulus are calculated from the previously determined critical porosity and for a range of gas saturation and sandstone porosity values.

Appendix B

Linear regression model

The linear regression model uses relationships between the bulk porosity, compressibility and shear modulus from fitted regression lines through a cloud of depth samples. It consists of the following operational steps:

1. For each depth sample within the target interval, the bulk porosity is calculated:

$$\phi_{bulk} = \frac{\rho_{solid} - \rho_{bulk}}{\rho_{solid} - \rho_{fluid}} \quad (\text{B-1})$$

2. Then compressibility is crossplotted against bulk porosity for all the samples within the target interval and a linear regression line is fitted through the cloud, resulting in the following relationship:

$$\kappa_{bulk} = a \cdot \phi_{bulk} + b \quad (\text{B-2})$$

3. Similarly, shear compliance is crossplotted against bulk porosity, giving the following relationship:

$$M_{bulk} = c \cdot \phi_{bulk} + d \quad (\text{B-3})$$

4. And lastly shear compliance is crossplotted against compressibility, resulting in the following linear regression relationship:

$$M_{bulk} = e \cdot \kappa_{bulk} + f \quad (\text{B-4})$$

5. For each crossplot, the coefficient of determination is computed (see Table 5-1), in order to investigate the reliability of each regression relationship. The two relationships resulting from the crossplots with the highest coefficient of determination are used in the further calculations.

6. For these two relationships, the slope (a , c or e) is used to compute the intercept (b , d or f) at each depth sample within the reservoir. For example:

$$b_z = \kappa_{bulk_z} - a \cdot \phi_{bulk_z} \quad (\text{B-5})$$

and:

$$f_z = M_{bulk_z} - e \cdot \kappa_{bulk_z} \quad (\text{B-6})$$

7. The bulk porosity is in/decreased percentage-wise with respect to its original value for each depth sample.
8. Finally, for each depth sample within the target interval the 'new' compressibility value is calculated. For example:

$$\kappa_{bulk,new_z} = a \cdot \phi_{bulk,new_z} + b_z \quad (\text{B-7})$$

9. And the 'new' shear compliance value is calculated for each depth sample within the target interval. For example:

$$M_{bulk,new_z} = e \cdot \kappa_{bulk,new_z} + f_z \quad (\text{B-8})$$